Multi-annual sub-pixel land cover mapping with TESSERA latent embeddings

Franz Schug[1,*], David Klehr[1], Jari Mahler[1,2], David Frantz[1]

[1] Geoinformatics - Spatial Data Science, Trier University, Universitätsring 15, 54296 Trier, Germany

[2] Environmental Remote Sensing and Geoinformatics, Trier University, Universitätsring 15, 54296 Trier, Germany

F. Schug*:	0000-0003-1534-5610	franz.schug@uni-trier.de
D. Klehr:	0009-0006-5461-1677	klehr@uni-trier.de
J. Mahler:	0009-0003-6899-2739	mahlerj@uni-trier.de
D. Frantz:	0000-0002-9292-3931	david.frantz@uni-trier.de

[*] Corresponding author

This is a non-peer-reviewed preprint submitted to EarthArXiv. This manuscript has been submitted for publication in Remote Sensing of Environment. Please note the manuscript has yet to be formally accepted for publication. Subsequent versions of this manuscript may have slightly different content. If accepted, the final version of this manuscript will be available via the 'Peer-reviewed Publication DOI' link on the right-hand side of this webpage.

Abstract

Mapping land cover in highly heterogeneous landscapes is challenging, and classifications have inherent limitations where the spatial resolution of remotely sensed data exceeds the size of small objects. Sub-pixel land cover fraction maps based on medium-resolution optical remote sensing data like Landsat or Sentinel-2 overcome this limitation but are often not consistently available across multiple years because creating temporally robust and comparable multi-class fraction models can be challenging. Latent embeddings from geospatial foundation models are promising as they represent high-dimensional, large-scale general-purpose spectral, temporal, and structural features derived from Earth Observation data that are largely independent of available high-quality observations at specific points in time. We here assessed the usability of TESSERA latent embeddings for machine-learning regression-based land cover fraction models and compared the performance to more conventional spectral-temporal metrics and spline coefficients as input features. We also assessed the suitability of these inputs to train temporally transferred and generalized fraction models. We found that TESSERA latent embeddings are a well-suitable input to land cover fraction mapping, performing slightly better than spectral-temporal-metrics-based models in many cases, both being notably outperformed by spline coefficients (MAE across classes and years 11.58 vs. 11.64 vs. 9.45). Spline coefficients also performed best in all temporally generalized and many temporally transferred models. However, models trained with TESSERA latent embeddings demonstrate the highest consistency of transferred models, highlighting their capability to handle data gaps. We suggest that TESSERA latent embeddings are a valuable input to fraction mapping where data availability across years is highly variable, but spline coefficients generally perform best when sufficient high-quality observations are available.

Keywords: regression-based fractions, neural network regression, spectral-temporal metrics, spline coefficients, mixed pixel, Sentinel-2, Sentinel-1

1. Introduction

Land cover maps are an indispensable tool for quantifying and interpreting the dynamics of both natural and human-shaped Earth surface processes. Accurate multi-temporal land cover data enables researchers, managers, planners, and policymakers to assess ecosystem changes and disturbances (Lewińska et al. 2021; Senf and Seidl 2021), monitor threats to biodiversity (Montero et al. 2021; Simkin et al. 2022), mitigate natural hazard exposure (Shao et al. 2020; Radeloff et al. 2023), and track hydrological changes (LaFontaine et al. 2015; Guzha et al. 2018).

Remote sensing excels at generating accurate land cover maps. Advances in processing power availability and data storage capabilities and the long-term continuity and open data policies of the Sentinel and Landsat archives (Drusch et al. 2012; Wulder et al. 2022) have driven progress in medium-resolution land cover mapping. The emergence of multi-temporal continental-to-global scale land cover products demonstrated that 10-30 m resolution imagery from Sentinel and Landsat is well-suited for producing reliable large-area maps of single (Marconcini et al. 2021; Potapov et al. 2022) and multiple land cover types (Venter et al. 2022; Xu et al. 2024) across years. However, many multi-temporal maps are categorical, where each pixel represents a single land cover class. This level of detail is often insufficient, for example in ecosystem research (Rioux et al. 2019) and ecology where spatial heterogeneity is a critical factor (Jackson and Fahrig 2015), and particularly in areas with small-scale patterns such as urban agglomerations or mediterranean-biome landscapes, where objects and features may be smaller than the pixel size of Landsat or Sentinel-2.

Sub-pixel fraction maps address the limitations of categorical maps by quantifying the share of distinct land cover types within each pixel, thereby better capturing surface complexity within mixed pixels. Since the introduction of linear spectral mixture analysis to remote sensing (Adams et al. 1986) and its application to multi-spectral Landsat imagery (Smith et al. 1990), several techniques have advanced sub-pixel fraction mapping. For instance, the substrate-vegetation-dark surface (SVD) mixture model decomposes a mixed pixel's spectral signal into three endmembers - substrate, vegetation, and dark surface - that physically represent a pixel's dominant spectral traits in multi-spectral data (Small 2004). The SVD model has proven universally applicable across space, time, and sensors (Sousa and Small 2019; Small and Sousa 2022; Small and Sousa 2023). Other concepts translate spectral data into more thematic land cover information, which is desirable for many applications (Ridd

1995; Phinn et al. 2002), and were refined with techniques that address spectral ambiguity between surface types and spectral variability within the same class, including multiple endmember spectral mixture analysis (Roberts et al. 1998), Monte Carlo-based pixel-wise endmember selection (Wetherley et al. 2017), ensemble learning (Okujeni et al. 2017), and machine learning-based fraction mapping approaches that effectively handle redundant training data (Okujeni et al. 2013). Furthermore, the limited three-dimensional feature space of multi-spectral imagery was expanded by, for example, using intra-annual time series data to exploit seasonal data variability to increase the number of identifiable surface types and quantify fractions of different vegetation types (Nill et al. 2022; Harkort et al. 2025) or even tree species (Klehr et al. 2025).

However, consistent multi-year fraction mapping with multi-spectral data remains a challenge. Among global land cover products, only few provide sub-pixel information, commonly so for a single class, such as built-up surfaces in the Global Human Settlement Layer (Pesaresi et al. 2024), and tree cover in Hansen et al. (2013). One reason is that the quality of fraction mapping is often directly impacted by data quality and availability. Even with open Landsat and Sentinel-2 data archives, high-quality observations are unevenly distributed across regions and time, often limited by clouds, cloud shadows, atmospheric disturbances, data acquisition priorities, or downlink limitations (Wulder et al. 2016; Zhang et al. 2022; Lewińska et al. 2024). Reflectance variations across years, driven by phenological shifts, droughts, or other climatic changes, further complicate the generation of temporally robust and comparable models for predicting fractions (Lewińska et al. 2025). Unlike image classification, fraction mapping is particularly vulnerable to reflectance variations because (a) the value range of fractions is continuous compared to the discrete nature of classification where the algorithm only determines a winning class, and (b) post-processing is more complex as rules for identifying implausible changes are less intuitive.

Previous research has demonstrated the value of multi-temporal medium-resolution land cover fraction mapping from multi-spectral data for monitoring land surface dynamics, often but not exclusively with a focus on vegetation cover (Jones et al. 2018; Suess et al. 2018; Kowalski et al. 2023; Okujeni et al. 2024). Several techniques reduced the impact of intra-annual data availability and quality on map performance, including limiting the image selection to periods of expected observation consistency like around peak vegetation greenness (Senf et al. 2020), incorporating multi-sensor data to increase intra-annual data density (Okujeni et al. 2024), or pixel-based image compositing which for each pixel merges phenologically similar observations to generate synthetic high-quality data when the original data have gaps (Vogeler et al. 2018). The Cumulative Endmember Fractions approach generates monthly fraction maps and sums fractions of a target land cover type, reducing the need for high-quality observations to one per month while accounting for illumination and phenological phases (Lewińska et al. 2020). Other studies condense multiple observations within a period into spectral-temporal metrics, that are statistical aggregations of reflectance values such as mean or maximum, to reduce the impact of missing data and improve model robustness and temporal transferability (Viana-Soto et al. 2022; Nill et al. 2022; Frantz et al. 2023; Pham et al. 2024). Alternatively, per-pixel function fitting was used to generate features that are insensitive to irregular data, such as through interpolation for observation gap filling (Stanimirova et al. 2022), regression modeling to smooth time series of fraction maps (Bullock et al. 2020; Chen et al. 2021), or by directly extracting features from weighted spline regression (Klehr et al. 2025). Finally, temporally generalized models, also referred to as signature extension (Woodcock et al. 2001), have shown promise for multi-annual fraction mapping by pooling training data from multiple years to represent various observation scenarios and phenological conditions (Senf et al. 2020; Pham et al. 2024). The ability to temporally transfer land cover models to years where no training data are available or to create temporally generalized models when training data originate from multiple years is essential because developing models for each year individually can be a labor-intensive or even impossible task. However, while all these approaches reduce the effects of sparse data, mapping performance may still be compromised when high-quality data availability is low or inconsistent (Bullock et al. 2020; Frantz et al. 2023).

Geospatial foundation models have recently emerged as an alternative means of deriving features for remote sensing machine learning applications. Geospatial foundation models are large-scale general-purpose neural networks, pre-trained on vast, diverse, and unlabeled Earth Observation data including but not limited to multi-spectral imagery using self-supervised learning (Mai et al. 2023). They capture spectral, temporal, and structural features of the Earth's surface and can be fine-tuned for specialized tasks like land-cover mapping (Xiao et al. 2025). Foundation models generate latent embeddings, which are high-dimensional but condensed non-linear representations of long-term satellite image time series, that implicitly retain all relevant semantic patterns in the data comparable to features in conventional remote sensing (Feng et al. 2025). Often based on transformer encoders, which capture relationships between data points independent of their distance to each other, latent embeddings are less sensitive to irregular or sparse data. This makes them potentially valuable for applications that are especially susceptible to variations in data availability, such as multi-temporal land cover mapping (Xiao et al. 2025). Notable examples for remote sensing foundation models applicable to land cover mapping include AlphaEarth (Brown et al. 2025), PRESTO (Tseng et al. 2023), or Prithvi (Szwarcman et al. 2024), with the research landscape rapidly evolving (Yang et al. 2025; Huang et al. 2025). Temporal Embeddings of Surface Spectra for Earth Representation and Analysis (TESSERA, Feng et al. 2025) is a recent foundation model providing pixel-based, global, gap-free, multi-annual latent embeddings at 10-m spatial resolution. TESSERA is distinguished by its accessibility and model transparency (Feng et al. 2025). While TESSERA embeddings have been successfully applied to tasks such as crop type mapping, neither TESSERA nor other geospatial foundation models have yet been investigated for land cover fraction mapping.

In this study, we empirically assessed the suitability of pixel-based latent embeddings from the TESSERA geospatial foundation model for multi-year sub-pixel land cover fraction mapping of *built-up surfaces*, *woody vegetation*, *non-woody vegetation*, *soil and rock*, and *water*. Specifically, we addressed the following research questions:

1. What is the accuracy of regression-based multi-class land cover fraction models using TESSERA latent embeddings?
2. How do the models generated with TESSERA embeddings compare to models based on more conventional approaches using spectral-temporal metrics and spline coefficients?
3. What is the performance of temporal model transfer and generalization across multiple years for all three approaches?

2. Data and methods

2.1. Study area

Our study area corresponds to the Military Grid Reference System tile 30UWE, covering approximately 10,000 km² of the Greater Manchester – Liverpool region in the United Kingdom (Figure 1). We selected this area because optical Sentinel-2, radar Sentinel-1, as well as TESSERA latent embeddings were consistently available between 2019 and 2024 at the time of data acquisition, providing six years of dense time series data for our study. The study area comprises a mix of land cover and land use types dominated by improved grassland (36.8%; all data from Rowland et al. 2025). It also includes urban (6.2%) and suburban (14.6%) areas along a gradient from large cities to smaller towns, broadleaved (9.1%) and coniferous (1.4%) woodland, arable land (8.2%), other grassland types (10.9%) as well as a variety of other heterogeneous land cover types such as fens, marshes, swamps, heathland, shrubs, and water bodies. The general land cover composition of the study area remained stable from 2019 to 2024. The area is part of a temperate climate biome.

[[FIGURE 1]]

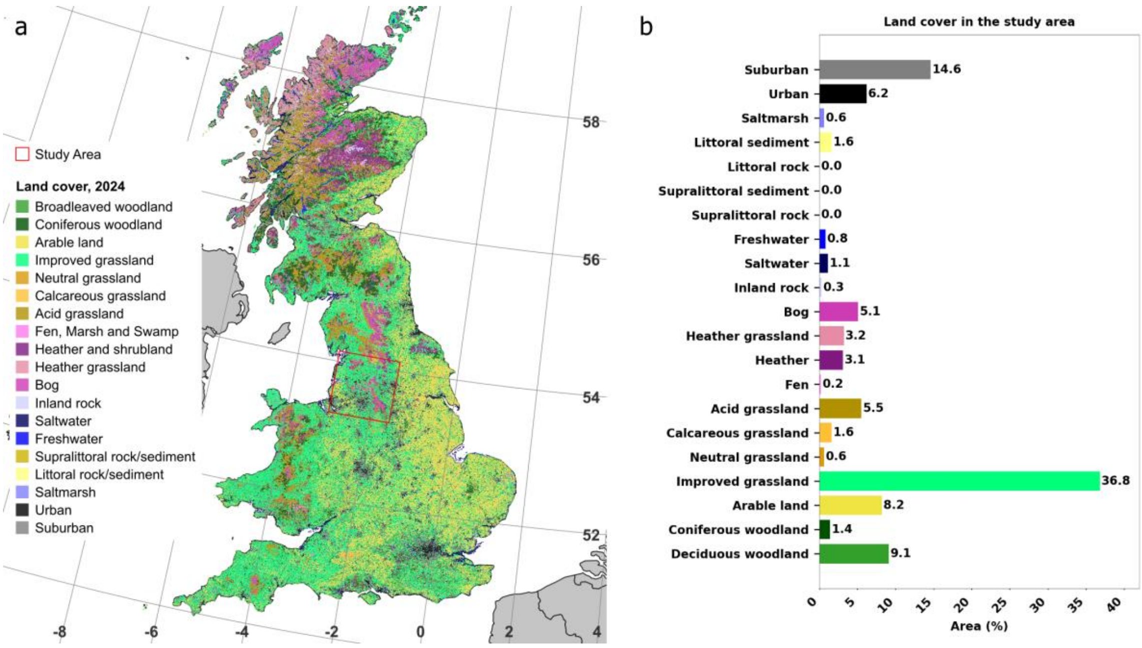

Figure 1 Study area: Military Grid Reference System tile 30UWE. Land cover representative for 2024 from Rowland et al. (2025). Country borders from www.naturalearthdata.com. CRS: EPSG 3035. b: Shares of land cover in the study area.

2.2.Data

Sentinel-2

We acquired all available optical Sentinel-2 A/B/C Level-1C data for 2019 to 2024 from Google Cloud Storage and the Copernicus Data Space Ecosystem. We limited our acquisition to images with less than 80% cloud cover because metadata cloud cover estimates do not include cloud shadows, cirrus clouds and cloud buffer areas, leading to very few usable image data when a higher threshold is used. We processed Sentinel-2 Level-1C data into analysis-ready-data using the open-source Framework for Operational Radiometric Correction for Environmental monitoring (FORCE, Frantz 2019). This process included radiometric, atmospheric, and topographic correction to produce high-quality standardized surface reflectance data (Frantz et al. 2016a), cloud and cloud shadow masking using parallax effect-based methods (Frantz et al. 2018), and the implementation of a data cube structure to enable efficient downstream analysis. We used Sentinel-2's visual, near infrared, and short-wave infrared bands (10 – 20 m resolution) and applied FORCE's ImproPhe algorithm to resample all data to 10-m resolution (Frantz et al. 2016b).

Across our study area, the median number of high-quality clear-sky observations per pixel ranged from 7 in 2024 to 12 in 2020, and the median maximum distance between clear-sky observations varied from 85 days in 2023 to 155 days in 2024 (see SI 1).

Sentinel-1

We also acquired analysis-ready monthly mosaics of Sentinel-1 radar data from the Copernicus Data Space Ecosystem for 2019 to 2024. These mosaics were generated from Sentinel-1 Ground Range Detected (GRD) observations in Interferometric Wide (IW) swath mode, using both VV and VH polarizations at 20 m resolution. The mosaicking process included backscatter coefficient calibration, thermal noise removal, and terrain correction following Small (2012), based on a weighted sum of backscatter observations, assigning higher weights to observations with the highest local resolution to minimize differences in backscatter caused by slope orientation and radar shadows. All data have been resampled to a 10-m spatial resolution to match Sentinel-2 image data using cubic convolution.

Temporal Embeddings of Surface Spectra for Earth Representation and Analysis

We acquired latent embeddings generated by the Temporal Embeddings of Surface Spectra for Earth Representation and Analysis (TESSERA) model for each year from 2019 to 2024. TESSERA is a pixel-oriented geospatial foundation model that uses self-supervised learning to create 128-dimensional, gap-free latent embeddings of optical Sentinel-2 and radar Sentinel-1 image time series at 10 m spatial resolution and global scale (Feng et al. 2025). Embeddings are generated using an encoder-projector framework. A dual-branch encoder processes the raw Sentinel-2 and Sentinel-1 time series separately to extract pixel-based key features using parallel transformer architectures. This process incorporates positional encoding based on the day-of-year of each observation to ensure temporal sensitivity. The model completely discards cloud-corrupted or low-quality observations. The 128-dimensional output of the initial encoding is expanded using a multi-layer perceptron to decorrelate data with a Barlow-Twins loss function (Zbontar et al. 2021), which reduces redundant information by retaining only the most informative features compressed in a 128-dimensional space.

A key advantage of TESSERA is the temporal stability and robustness of its embeddings. This is achieved because the model utilizes random temporal sampling to simulate invariance across time series affected by missing data. Additionally, training data is globally shuffled to reduce the impact of spatially autocorrelated data (Feng et al. 2025). This makes it a promising dataset for multi-year land cover fraction mapping. Additionally, TESSERA offers advantages over other foundation models as it provides analysis-ready, gap-free, global, and annual embeddings at 10-m spatial resolution and pixel-level, derived from an openly accessible model (Feng et al. 2025). TESSERA embeddings have been successfully applied to downstream tasks such as land cover and crop type mapping, canopy height estimation, above-ground biomass prediction, and burned area detection (Feng et al. 2025; Timoner et al. 2026).

Land cover

We used land cover reference data for 2024 provided by the UK Center for Ecology & Hydrology (UKCEH). This dataset consists of a pixel-wise classification of 21 distinct land cover and land use types derived from Sentinel-2 satellite imagery at a 10-m spatial resolution. These data were not used during model training or prediction but, with an overall accuracy of 83%, served as a starting point for identifying locations to extract training data for our analysis (Figure 1, Rowland et al. 2025).

2.3. Methods

Workflow

We compared three approaches to mapping land cover fractions of built-up surfaces, woody vegetation, non-woody vegetation, soil and rock, and water. We implemented an established workflow to multi-temporal land cover fraction mapping (Nill et al. 2022; Pham et al. 2024) based on machine learning regression models and synthetically mixed signatures along with random reference fraction ratios for training. We used spectral-temporal metrics, spline coefficients, and TESSERA latent embeddings as inputs for model training and prediction. For each target year (2019-2024), we evaluated the performance of three configurations: a) models trained on data from the target year, b) models trained on data from each non-target year to assess temporal model transferability across years, and c) models trained on data from all non-target years combined to assess model generalizability.

Spectral-temporal metrics

We computed spectral-temporal metrics from Sentinel-2 analysis-ready reflectance time series and monthly Sentinel-1 backscatter mosaics. Spectral-temporal metrics are temporal data aggregations that collapse all available observations within a period into band-wise summary statistics, such as mean or maximum reflectance (Frantz et al. 2023). They represent gap-free, ready-to-use data eliminating the need for manual observation selection and facilitating data comparison across large areas and time when observation availability varies. Spectral-temporal metrics implicitly retain temporal information when combining different metrics, such as minimum and maximum reflectance that represent spectral properties in different seasons. Temporally aggregated image data have been successfully applied across diverse remote sensing applications such as forest cover monitoring (Potapov et al. 2015), land cover classification (Azzari and Lobell 2017; Pflugmacher et al. 2019), cropland mapping (Phalke and Özdoğan 2018), and building height quantification (Frantz et al. 2021). Spectral-temporal metrics are also well-suited for land cover fraction mapping, especially over large areas (Pfoch et al. 2026), multiple sites (Schug et al. 2024), and multiple years (Pham et al. 2024).

We generated pixel-wise annual spectral-temporal metrics from all high-quality Sentinel-2 observations (i.e., cloud-, cloud shadow-, snow-, and saturation-free) acquired between January 1^{st} and December 31^{st}. We computed the 25th and 75th percentile and mean reflectance for all spectral bands, representing the average surface state and seasonality. We also computed the 90th percentile of the Normalized Difference Vegetation Index (NDVI, Tucker 1979) and Tasseled Cap Greenness (TCG, Kauth and Thomas 1976) to better capture seasonal vegetation with only a short green peak. We computed the 10th and 90th percentile and mean backscatter of VV and VH polarized Sentinel-1 monthly mosaics to approximate seasonal surface roughness variation and to mirror the sensor combination used for TESSERA embeddings (Feng et al. 2025). In total, we used 38 features to train our models.

Although spectral-temporal metrics are generally robust to image availability variability, insufficient high-quality observations can negatively affect this robustness. Because of high observation variability in our study area, we adopted the random observation selection approach following Pham et al. (2024). This approach generates additional spectral-temporal metric sets by randomly sampling 80%, 60%, 40%, and 20% of available clear-sky observations per year, simulating low-data-density scenarios during training. Random observation selection consistently improved the quality of land cover fraction mapping, particularly for temporal model transfer and generalization (Pham et al. 2024).

Spline coefficients

We also applied weighted spline fitting for each year of analysis following Bolton et al. (2020). Weighted spline fitting reconstructs intra-annual time series data by fitting spline coefficients to analysis-ready data time series. Thus, the approach generates temporally consistent representations of intra-annual surface and vegetation dynamics and mitigates the effects of observation gaps by fitting spline coefficients to the time series of band-wise reflectance. The concept of spline fitting has been successfully applied to, for example, tree species mapping (Klehr et al. 2025). First, we identified a weighing scheme that defined the impact of each observation on spline fitting. Observations from the target year received a weight of 1. Additionally, we included observations from the two preceding years, receiving weights of 0.30 and 0.15, respectively. This is to make sure that observations from the target year dominated the fit whenever sufficient data were available, but that observations from previous years could be included to fill data gaps in the target year. Second, the initial weights were refined using a residual-based weighting scheme: To do so, a preliminary cubic b-spline was fitted to an NDVI time series constructed from all available observations for each year. Relative residuals between observed and fitted NDVI values were then used to reduce the weights of observations that deviated strongly. This procedure reduced the influence of outliers and observations inconsistent with the dominant phenological pattern. Third, the resulting weighted observations were used to fit a spectral time series. For each Sentinel-2 spectral band, we fitted a cubic smoothed b-spline with 22 coefficients and fixed breakpoints distributed across the target year. We controlled spline smoothness using a regularization parameter, which penalized excessive curvature of the fitted function. To stabilize spline estimates at the start and end of the year, we padded three additional observations before and after the annual time series using median values derived from edge observations. We added annual average backscatter from Sentinel-1 to the spline coefficients to match the sensor combination used for TESSERA embeddings. The spline coefficients provided consistent input variables across the entire study area, which is required for regression-based fraction mapping. We implemented the approach using the GNU Scientific Library (https://www.gnu.org/software/gsl/). The source code of the time-series parameter extraction workflow is publicly available on GitHub (https://github.com/ForestPulse/splinecoefs).

Training data locations

Our approach requires training data that captures the spectral characteristics of all target surface types. We used UKCEH land cover reference data for 2024 (Rowland et al. 2025) to identify candidate locations for training data (see Table-SI 2). We reclassified the 21 UKCEH land cover classes into ten classes that are visually identifiable using aerial or satellite data. For these ten classes, we manually identified locations where land cover was invariant within and across years and where each pixel represented a single land cover type (*pure pixel*) with the support of 2024 Google Earth VHR imagery and 90th percentile NDVI values. Vegetation sites required a 90th percentile NDVI ≥ 0.7 in all years since 2019 (> 0.3 for non-vegetated land cover). In total, we identified 468 training locations, with a minimum of 30 per class (Table 2), which we translated into our five target classes built-up surfaces, woody vegetation, non-woody vegetation, soil and rock, and water.

[[TABLE 1]]

Table 1 Number of locations for training data sampling per sampling class and associated target class.

Target Class	Sampling Class	Locations
Impervious surface	Building	66
	Road and rail	69
Woody vegetation	Deciduous woodland	47
	Coniferous woodland	31
Non-Woody Vegetation	Arable land	52
	Improved grassland	45
	Other grassland	33
	Bog, fen, and marsh vegetation	52
Soil and Rock		30
Water		43
Total		468

Regression-based fraction mapping with synthetically mixed training data

At the training locations, we extracted features from the spectral-temporal metrics including the random observation selection subsets, the spline coefficients, and from TESSERA latent embeddings to create three separate signature libraries associated with the five land cover types. For each library and year, we generated synthetically mixed training data for regression-based model training, which requires reference data for mixed land cover to fit a regression function. We generated 128,000 synthetic signatures per library, respectively, using randomly defined mixing ratios of one to three randomly drawn signatures from different or the same land cover type (see example in Figure-SI 3). Using synthetically mixed signatures along with their mixing ratios as dependent variables for regression training, a small representative sample of pure pixels is sufficient to derive training data representing a wide range of mixed pixel scenarios (Okujeni et al. 2013; Stanimirova et al. 2022; Viana-Soto et al. 2022; Schug et al. 2024). We used a neural network regressor with multi-target prediction as implemented in the *Keras* package for *Python 3* (Gullì and Pal 2017), previously shown to be well-suited for regression-based fraction mapping (Pham et al. 2024; Schug et al. 2024; Klehr et al. 2025). Model output consisted of percent fractions for each land cover type, capped to between 0-100% during post-processing. Following Pham et al. (2024), the neural network architecture consisted of two hidden layers (512 nodes each), a mean absolute error loss function, and an Adam optimizer (Kingma and Ba 2014) with an initial learning rate of 0.001 over 50 epochs.

Using spectral-temporal metrics (*STM approach*), spline coefficients (*spline approach*), and TESSERA embeddings (*TESSERA approach*) as predictors, we mapped land cover fractions for each year (2019–2024) under three configurations:

a. *Same-year models* using training data from the target year
b. *Temporally transferred model* using training data from all non-target years separately
c. *Temporally generalized models* with pooled training data from all non-target years combined

Validation

We systematically assessed the accuracy of our results by comparing fraction estimates of built-up surfaces, woody vegetation, and non-woody vegetation with expert-derived reference fractions from Google Earth VHR data. Although used for model training, water and bare soil were not validated because they were insufficiently represented in the study area. We used stratified random sampling to identify 450 validation pixels following Schug et al. (2024). Based on the 2024 same-year Sentinel-based fraction estimates, we defined ten fractional bins in steps of 10% per class and randomly allocated 15 validation pixels to each bin, resulting in 150 sites per class equally distributed between 0 and 100% fraction. To minimize spatially dependent mapping errors, we maintained a minimum 500 m distance between validation pixels. We replaced pixels with ≤ 2 clear-sky Sentinel-2 observations in any year (2019-2024) or where historical Google Earth VHR imagery revealed unstable land cover, for example due to construction or deforestation, to keep a single validation dataset for all years. We eventually replaced 12 validation pixels.

We performed validation at a resolution of 30 m to facilitate comparison with similar studies (Figure 2). We generated a regular 11 x 11-point grid per validation pixel, where the 9 x 9 center points aligned with a 10-m pixel and its eight adjacent pixels (Queen contiguity), representing 30-m resolution. The full 11 x 11-grid was used for an extended validation accounting for both potential geolocation error and possible misalignment between fractions and Google Earth VHR data. We assigned each point in the grid a land cover type and calculated reference fractions based on the number of points labelled with a type. We used VHR data from Google Earth for 2024, supplemented by Sentinel-2 NDVI data where land cover was ambiguous, for example when the landscape structure suggested agriculture, but VHR data displayed bare soil.

Model performance was evaluated using mean absolute error (MAE), slope, and the coefficient of determination (R^2) for all same-year, temporally transferred, and temporally generalized models based on the STM, spline, and TESSERA approach, respectively.

[[FIGURE 2]]

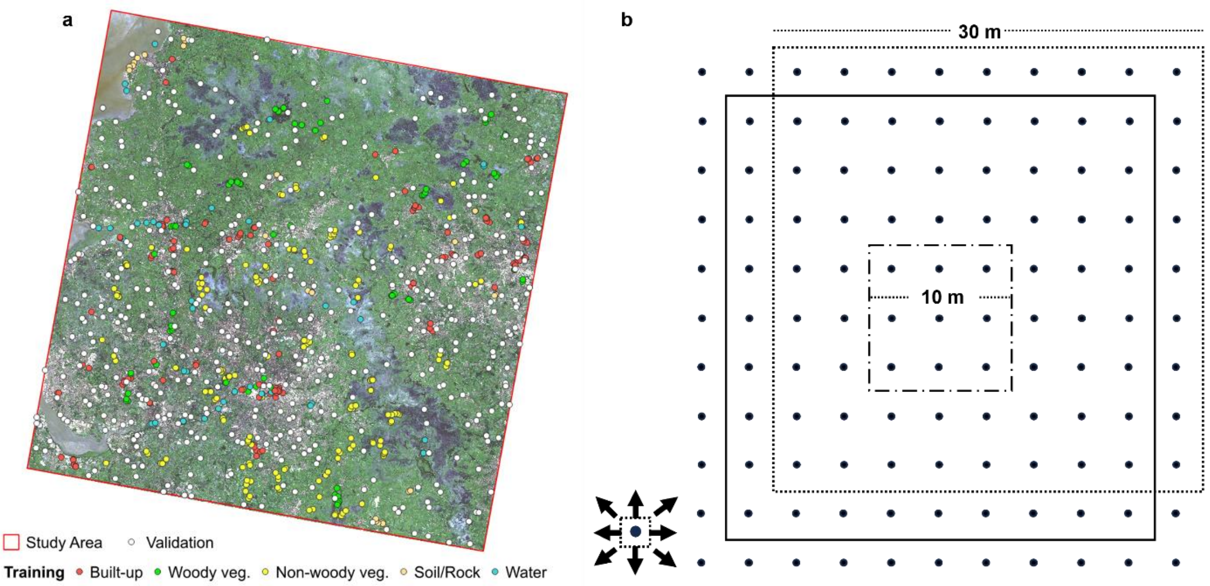

Figure 2 a) Study area including all training (n = 468) and validation (n = 450) locations. Background: Median red, green, blue reflectance of 2024 at 70% opacity. b) Validation scheme: We labeled land cover at 11 x 11 points. We compared our predicted results with the reference surface fractions of 9 x 9 points, i.e., the shares of each land surface type within 30-m of

the center pixel (solid line). We also compared our maps to the reference surface fractions of 9 x 9 points when the reference is shifted by one point into each direction (Queen contiguity), accounting for potential misalignments and geolocation errors.

3. Results

We accurately predicted land cover shares of built-up surfaces, woody vegetation, and non-woody vegetation in each year from 2019 to 2024 using spectral-temporal metrics, spline coefficients, and TESSERA latent embeddings as input features to regression-based fraction mapping (Figure 3). Using the same-year model for 2024 as an example, all three approaches yielded similar results with the lowest MAE between 6.94 and 9.77 for built-up surfaces and the highest between 11.17 and 14.17 for non-woody vegetation (Figure 4), an R^2 between 0.71 and 0.88 across all surface types, and slopes close to 1. The spline approach had the best MAE and R^2 values across the classes. However, the TESSERA approach had the best slope values, i.e., closest to 1. The extended validation showed that slight potential pixel shifts would only marginally affect the results, but the effects seem higher in the TESSERA approach (see Figure-SI 4).

[[FIGURE 3]]

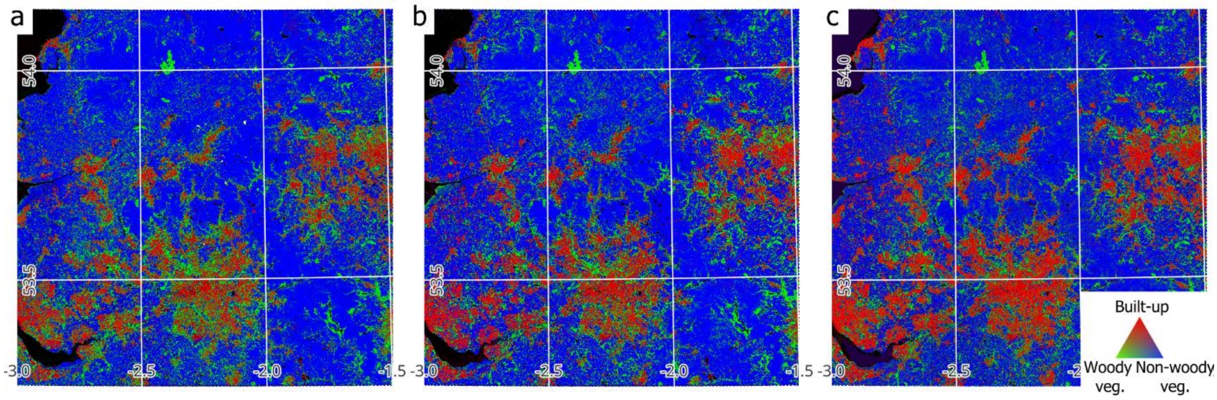

Figure 3 Predicted land cover fractions of built-up surfaces (red), woody (green) and non-woody vegetation (blue) using Sentinel-based spectral-temporal metrics (a), spline coefficients (b), and TESSERA latent embeddings (c). Model: same-year model for 2024.

The validation of same-year models for other years revealed that across all years and with only few exceptions, the spline approach yielded the lowest MAE, highest R^2, and best slope values when averaging all land cover types (Figure 5). Compared to the lowest performing approach, the spline approach reduced the MAE by ca. 20% across all years. This pattern is confirmed for each land cover type where the spline approach yields the best MAE in 14 of 18 cases (6 years x 3 classes), best R^2 in 18 of 18 cases, and best slope in 9 of 18 cases (see SI

4). The STM approach is performing less well especially for woody vegetation surfaces, and the TESSERA approach tends to show high MAE values for non-woody vegetation.

[[FIGURE 4]]

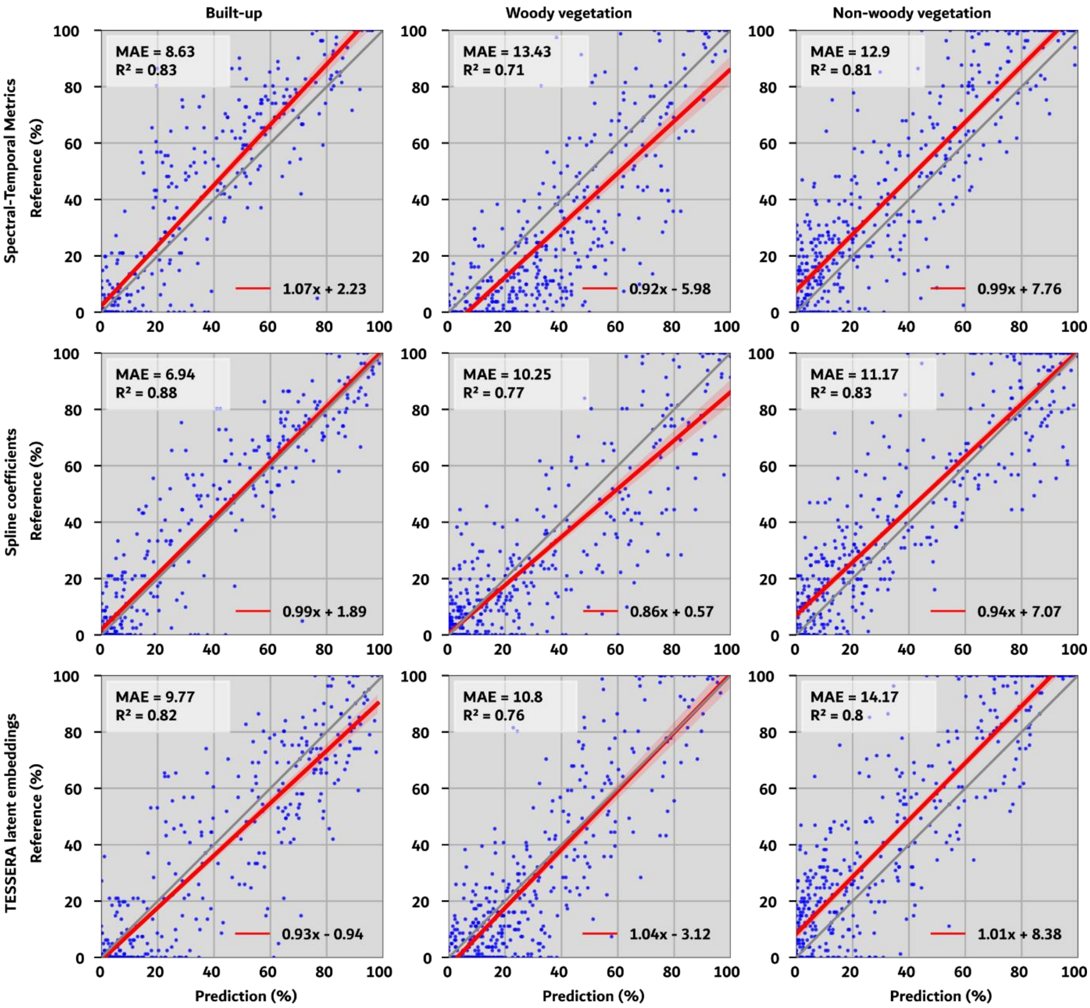

Figure 4: Performance of land cover fraction models based on spectral-temporal metrics (top), spline coefficients (center), and TESSERA latent embedding (bottom) for built-up, woody vegetation, and non-woody vegetation surfaces. Example of same-year models for 2024.

The validation of temporally transferred models revealed overall similar patterns. Across the years and land cover types, the spline approach yielded lowest MAE values in 56 of 75 cases (5 years of training x 5 years of prediction x 3 classes). TESSERA performed best in 20 cases, all of which were woody vegetation, and STMs performed best in 15 cases, 12 of which in non-woody vegetation. The spline approach yielded best R^2 values in 47 of 75 cases (TESSERA 25, STMs 18). However, TESSERA-based models showed the best slope values in 45 cases (splines 39, STMs 12). There is a temporal pattern based on the year of training, as, for example, the TESSERA approach performed best 12 of 15 times in 2024, but only 3 times in 2019. TESSERA-based models were also considerably more robust across the years.

First, this was indicated by fewer outliers. While with the STM approach, 31 of 108 models across all years and classes (including same-year models) had an $R^2 < 0.7$ and 54 models had slopes < 0.9 or > 1.1, these numbers were only 3 and 24 with the TESSERA approach (6 and 35 for splines). Second, the quality of TESSERA-based models was more consistent, both when the quality metrics were aggregated by year of training and year of prediction (Figure 6). The average MAE of all three classes was lowest using the spline approach in almost every year, both when aggregating the results by year of training (i.e., considering all predictions created with training data from a certain year) and by year of prediction (i.e., considering all predictions in a certain year with models from all other years, respectively). However, the results of the TESSERA approach yielded the lowest MAE variability, with a standard deviation of 0.36 and 0.35 for the aggregation by year of training and prediction, respectively, compared to the spline approach with standard deviations of 0.78 and 0.53. The MAE of the STM approach varied considerably with standard deviations across the years of 1.4 and 0.76. While not as pronounced, we found similar patterns for R^2 and slope, and the patterns also applied for all three classes individually (see SI 5).

[[FIGURE 5]]

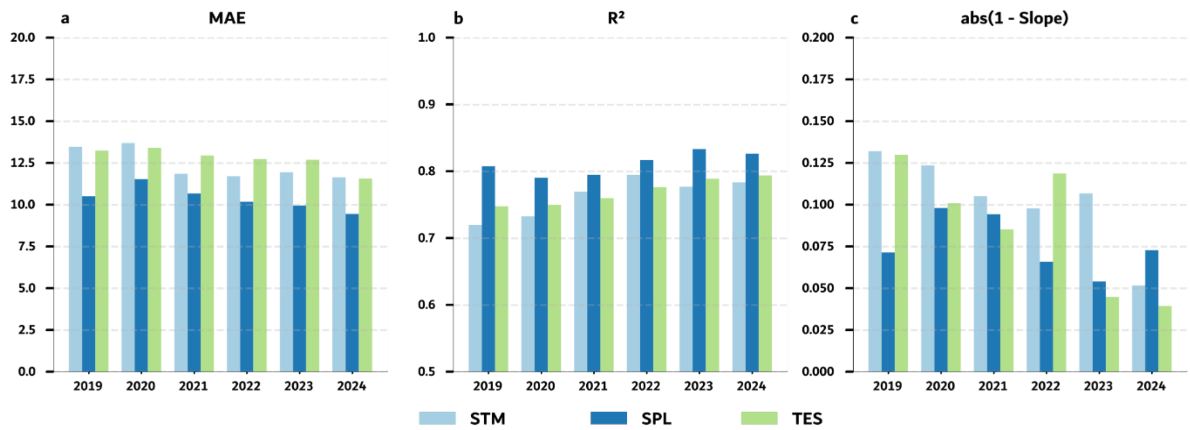

Figure 5 Mean absolute errors (a), coefficients of determination (b), and slope (c) averaged across all classes for all same-year models and all three approaches. STM: Spectral-temporal metrics, SPL: Spline coefficients, TES: TESSERA latent embeddings.

The analysis of temporally generalized models was largely in line with the same-year model results. Again, the spline approach consistently performed best regarding MAE, R^2, and Slope for all classes combined (Figure 7) as well as for all classes individually (see SI 4). Compared to the STM approach, the TESSERA approach often showed lower MAE values for woody vegetation surfaces and considerably increased R^2 for models where the STM approach underperformed (i.e., $R^2 < 0.7$). Again, the TESSERA approach yielded higher model consistency across the predicted years. For example, the standard deviation of the MAE for built-up, woody vegetation, and non-woody vegetation surfaces was 0.55, 0.43, and 0.21 for the TESSERA approach, compared to 1.38, 1.07, and 0.55 for the STM and 0.60, 0.46, and 0.50 for the spline approach. The spline and TESSERA approaches additionally show very high consistency across the years in how the fraction errors in generalized models are distributed (**Figure *8***, Table 3).

[[FIGURE 6]]

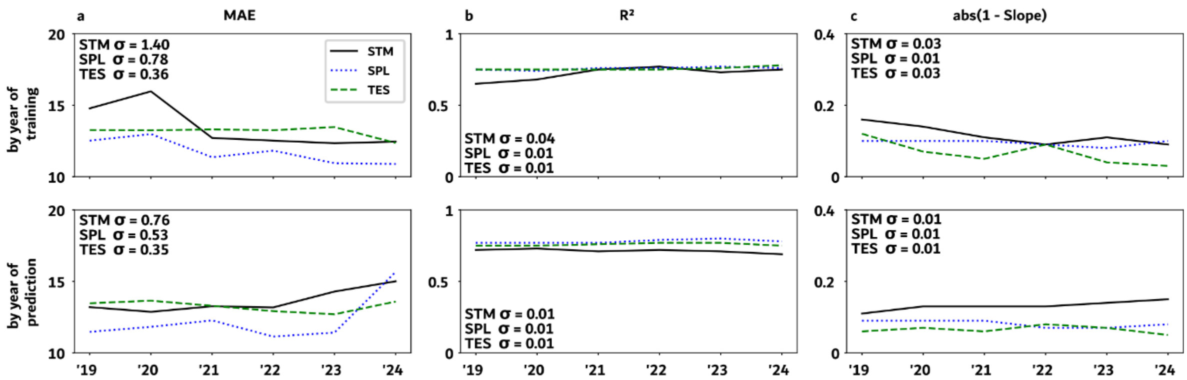

Figure 6 Mean absolute error (a), coefficient of determination (b), and Slope (c) averaged across all classes for all years, aggregated by year of training (top) and year of prediction (bottom). STM: Spectral-temporal metrics, SPL: Spline coefficients, TES: TESSERA latent embeddings, σ: Standard deviation.

[[FIGURE 7]]

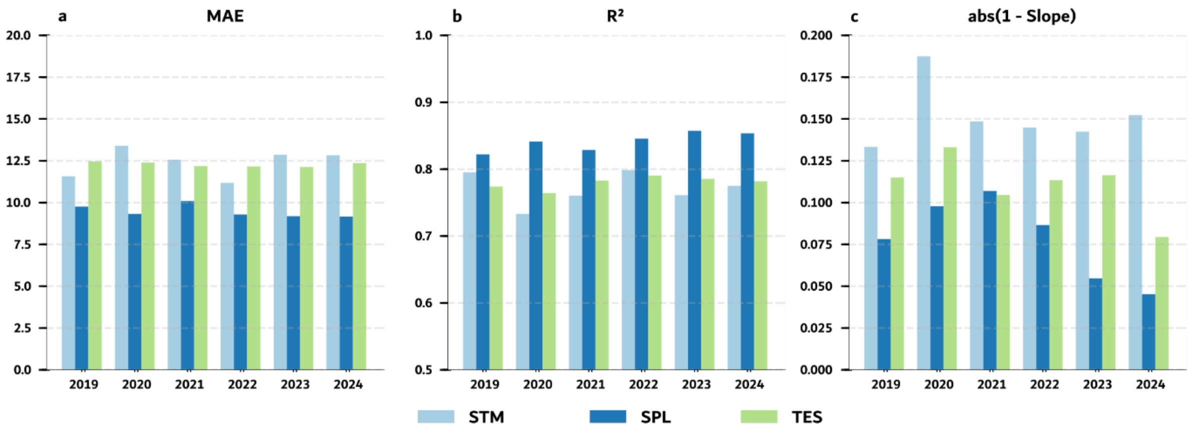

Figure 7 Mean absolute errors (a), coefficients of determination (b), and Slope (c) averaged across all classes for all temporally generalized models and all three approaches. STM: Spectral-temporal metrics, SPL: Spline coefficients, TES: TESSERA latent embeddings.

[[TABLE 2]]

Table 1 Class-wise mean and standard deviation of cumulative areas between the curves and axes across all years and approaches for temporally generalized models. Cumulative area between the curve and axis describes the difference between the density plots of 1) all reference fractions in the 450 validation points and 2) the mapped fractions of the temporally generalized model in these same validation points. The lower the means, the closer the distribution of predictions is to the distribution of reference fractions. The lower the standard deviations, the more consistent are the model predictions given that the references are assumed to be temporarily invariant. **Bold**: Best result per class. STM: Spectral-temporal metrics, SPL: Spline coefficients, TES: TESSERA latent embeddings

	Mean			Standard deviation		
Class	**STM**	**SPL**	**TES**	**STM**	**SPL**	**TES**
BU	0.183	**0.140**	0.156	0.012	0.015	**0.011**
WV	0.349	**0.210**	0.262	0.039	0.041	**0.029**
NWV	0.197	**0.166**	0.236	0.013	**0.012**	**0.012**

[[FIGURE 8]]

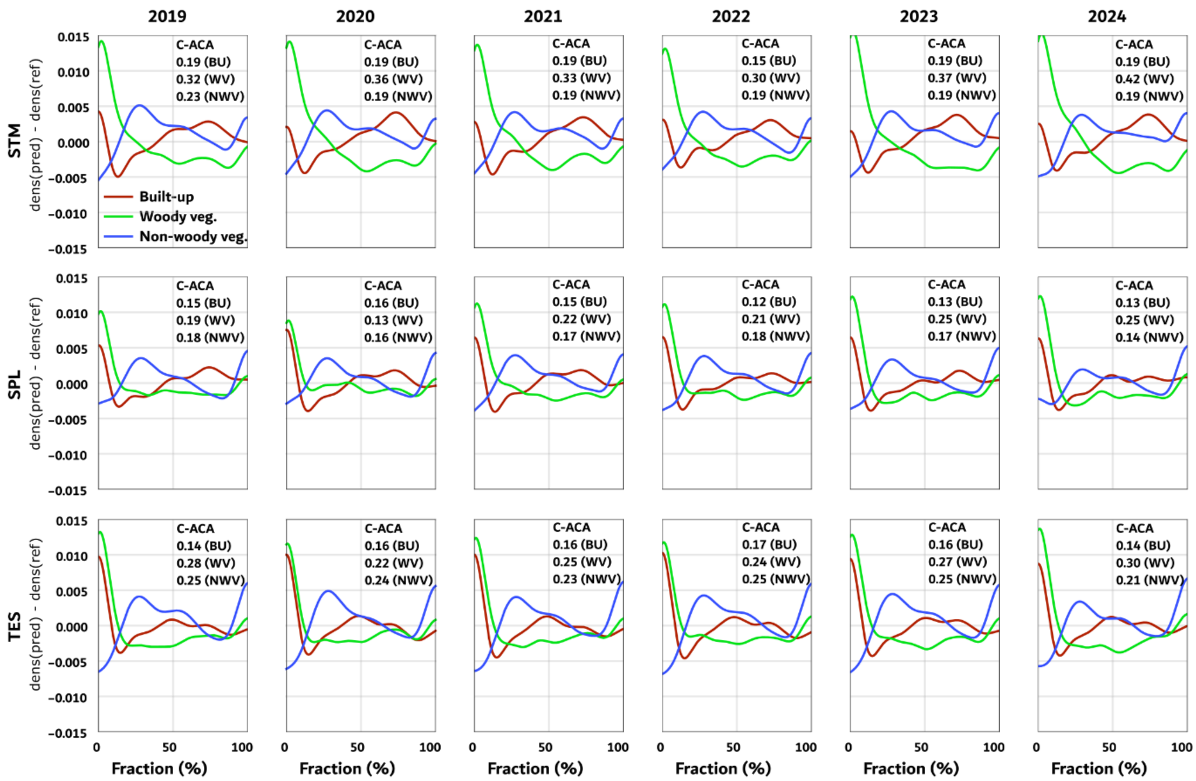

Figure 8 Difference of density plots of 1) all reference fractions in the 450 validation points and 2) the mapped fractions of the temporally generalized model in these same validation points for each class, each approach, and each year. The validation points were considered temporally invariant, which is why the difference to the distribution of mapped fractions was considered an error, and any changes in that difference across the years were considered an effect of model performance. Thus, a consistent area under the curve indicates a temporally consistent model performance. STM: Spectral-temporal metrics, SPL: Spline coefficients, TES: TESSERA latent embeddings, C-ACA: Absolute cumulative area between curve and axis. The lower the C-ACA, the closer the distribution of predictions is to the distribution of reference fractions. The more

consistent the C-ACA is across years, the more consistent are the model predictions given that the references are assumed to be temporarily invariant.

Beyond systematic validation, visual inspection of our maps confirms the generally good quality of all approaches. This is important because some mapping challenges might not be reflected in the validation when they are associated with highly autocorrelated data which was not sampled for validation to avoid skewed quality metrics. For example, the TESSERA approach yielded more accurate results in dense urban areas where the STM approach is challenged by year-round low-reflectance building shadows and tends to map high fractions of water (**Figure *9***a). Unlike the STM and the spline approaches, TESSERA-based models are also not challenged by data gaps when insufficient observations are available (**Figure *9***b). The STM approach produced more plausible results for low wetland vegetation (Figure 9e) and seemed to map managed grassland more consistently (**Figure *9***f). In contrast, the spline approach mapped vegetation in dense suburban areas more reliably where STM- and TESSERA-based models tended to over- and underestimate fractions, respectively (**Figure *9***d).

[[FIGURE 9]]

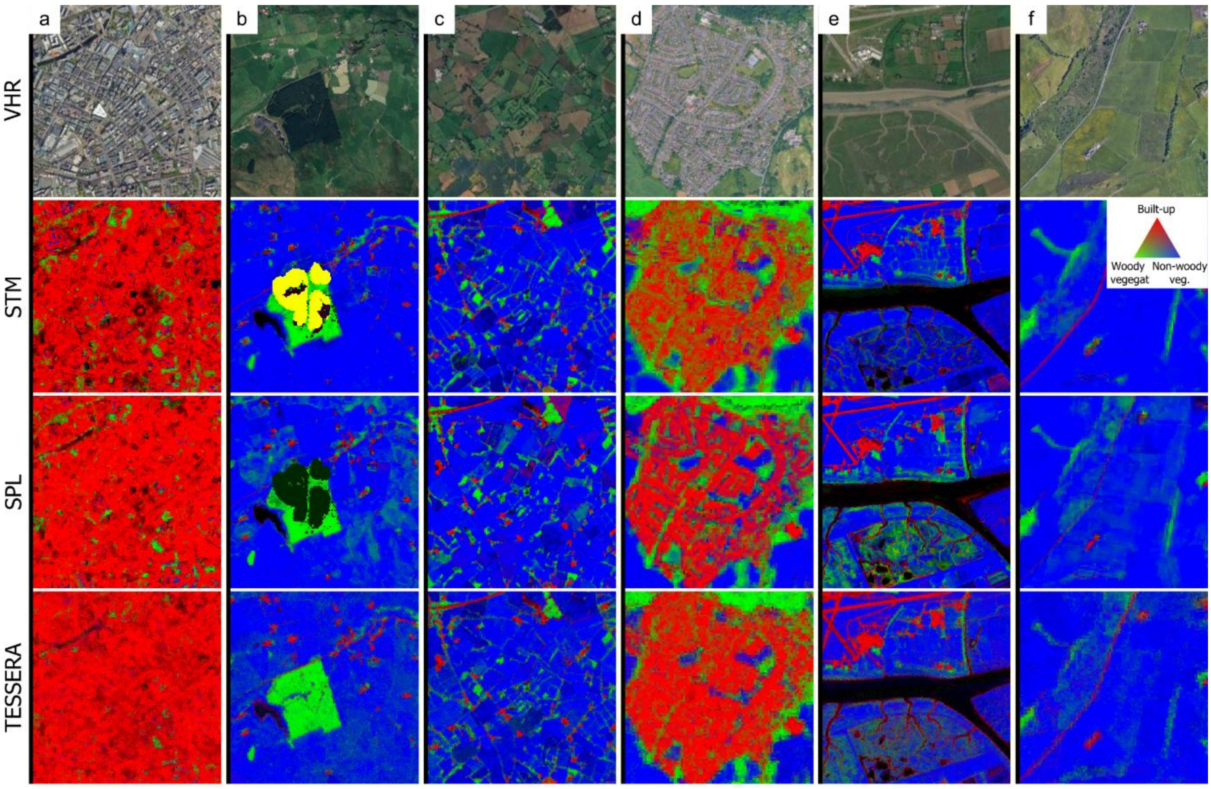

Figure 9 Examples of land cover fraction maps of built-up surfaces (red), woody-vegetation (green), and non-woody vegetation (blue) across the study area in urban, suburban, forested, managed agriculture and grassland, and wetlands. Yellow: No data.

4. Discussion

We found that latent embeddings from the TESSERA geospatial foundation model accurately predict fractions of built-up surfaces, woody, and non-woody vegetation using regression-based mapping and synthetically mixed training data. In same-year models, latent embeddings performed comparably to spectral-temporal metrics, though both were often outperformed by spline coefficients in terms of mean absolute error and coefficient of determination. Our same-year model performance aligned with prior studies, despite variations in sensors, data sources, class catalogues, study areas, and temporal scope (Schug et al. 2020; Nill et al. 2022; Viana-Soto et al. 2022; Pham et al. 2024; Schug et al. 2024; Lobert et al. 2025). All our three approaches excelled where land cover classification is challenged, such as low-density vegetation-rich built-up areas and heterogeneous landscapes like heathlands or pasture smallholdings, but all approaches struggled in some classes and settings. Visually, this stood out where errors were highly autocorrelated, that means where contiguous areas of similar surfaces were inaccurately mapped but not captured by the validation. This was expected and previously reported for the STM approach (Schug et al. 2024).

While STMs have previously excelled in temporal model transfer and generalization (Senf et al. 2020; Pham et al. 2024), spline coefficients consistently outperformed both STMs and TESSERA across all classes, delivering the most accurate predictions. However, slope metrics indicated that TESSERA-based models offered more stable predictions across the value range of predicted fraction. Importantly, temporally transferred TESSERA-based models exhibited the lowest variation in quality metrics across years, regardless of year of training or year of prediction. This supports the assumption that TESSERA embeddings are less susceptible to temporal data inconsistency but also makes potential errors easier to diagnose and correct for even when the overall performance was lower than that of the spline-based models. Temporally generalized models often matched same-year model performance, supporting previous research (Kowalski et al. 2023), with spline-based models again performing best. For generalized models, both spline and TESSERA approaches demonstrated high stability in predicted fractions over time.

Despite their distinct feature characteristics and modeling results, STMs, spline coefficients, and TESSERA embeddings are all valuable inputs for land cover fraction modeling. Spectral-temporal metrics (STMs) offer an intuitive rationale to data aggregation using simple statistical metrics that implicitly retain phenological information (Frantz et al. 2023). STMs are computationally efficient, mostly insensitive to regional phenological variation, and STM-based models are generally transferable across global biomes (Schug et al. 2024). However, their quality depends on intra-annual high-quality image availability. While only a few observations suffice to derive usable features, imperfectly distributed observations reduce temporal feature consistency (Frantz et al. 2023) and mapping quality (Pham et al. 2024). This influences temporally transferred models in particular. Furthermore, feature selection for model training remains non-trivial (Schug et al. 2020).

Spline coefficients represent spectral-temporal trajectories as mathematically modeled coefficients of a higher-dimensional polynomial curve. Spline coefficients are a transparent and intuitive representation of intra-annual phenology but, unlike STMs, require upstream modeling and parameterization. The approach includes observations from previous years (Bolton et al. 2020), but even then some years failed to provide enough data such as 2017 and 2018. Within our study area, the spline approach provided the best results, but as spline coefficients represent phenological information explicitly, it is unclear how the approach performs across large and climatically heterogeneous areas. Explicit phenological information could, however, support resolving confusion where intra-annual land cover variation is high such as in agriculture.

TESSERA-based models offered exceptional temporal stability, especially in temporally transferred models. TESSERA's 128 features are a complex representation of intra-annual Earth surface processes but are independent of the temporal distribution of observations (Feng et al. 2025). However, TESSERA's interpretability is limited, and the TESSERA feature space is less intuitive compared to STMs or spline coefficients. TESSERA embeddings are almost globally available for multiple years, but users rely on the availability of the data in their region, year of interest, and the version of their choice. TESSERA is an open-source ecosystem, but generating embeddings is computationally expensive. TESSERA's consistency makes it promising for global applications, but spatial transferability as well as the use of implicit phenological information for intra-annual mapping remain unexplored in comparison to alternative approaches such as cumulative endmember fractions (Lewińska et al. 2021) or temporal mixture models where endmembers are selected based on their seasonal characteristics (Sousa and Davis 2020).

All three tested approaches share advantages and challenges. For instance, they provide thematically interpretable information as opposed to the global SVD endmember model (Small and Milesi 2013) and higher class complexity than the original multi-spectral mixing space (Small 2004). Our use of a single multi-class regressor is a reduction in complexity compared to class-specific regressors used in previous studies (Okujeni et al. 2013). Furthermore, the STM and spline approaches can be applied to Landsat data extending back to the 1970s/1980s, and while TESSERA embeddings are not currently computed for Landsat, doing so is likely feasible in the future. Challenges persisted in areas with high surface seasonality such as agriculture. Here, intra-annual changes were often interpreted as spatial mixtures, even when explicit phenological information was available in the spline approach. Furthermore, identifying pure pixels for training was sometimes challenging, such as for roads and railroads. Supplementing training data from existing libraries might improve model performance, particularly in urban settings characterized by high spectral-spatial heterogeneity (van der Linden et al. 2018). Endmember extraction algorithms (Jilge et al. 2017) or generic libraries (Priem et al. 2025) could facilitate the training process. While we used an established validation framework without the need for on-the-ground data collection (Schug et al. 2020), the validation was possibly confounded by shifted very-high resolution imagery, geolocation errors of up to 12 m in Sentinel-2 data from before 2021 (Gascon 2019), and visible pixel shift in the TESSERA data. However, we quantified the potential error of image shifts by employing a larger validation grid and found that related errors were low. Lastly, despite a rigorous validation procedure, actual feature stability is hard to test, as we cannot exclude that differences in prediction quality came from varying observation scenarios. The exact effect of irregularly distributed image observations on mapping quality in the three approaches is yet uncertain.

5. Conclusion

Spectral-temporal metrics, spline coefficients, and TESSERA latent embeddings all enable high-quality land cover fraction mapping despite the distinct ways in which the data are generated. This highlights the robustness of regression-based fraction mapping. However, each approach has its strengths and limitations. We recommend the use of spectral-temporal metrics when the temporal scope of the analysis is limited to a single year or multiple years with similar observation scenarios, input data are consistently distributed within a year, computational resources are critical, or when interpretability is a priority. We recommend the use of spline coefficients when targeting the best map quality, when the available training data are from different years, sufficient high-quality observations data are available, and when the phenological characteristics within the study area are consistent. We recommend the use of TESSERA latent embeddings when temporally consistent fraction predictions are required but when feature interpretability is not critical. TESSERA is ideal for expanding existing models to years without training data, though reproducibility of input features may be limited without considerable computational resources.

Acknowledgements

Competing interests statement

The authors declare that they have no known competing interests.

Data availability statement

Data will be made available on request.

CRediT author contribution statement

F. Schug: Conceptualization, Data curation, Formal analysis, Investigation, Methodology, Validation, Writing – original draft

D. Klehr: Visualization, Writing – review and editing

J. Mahler: Visualization, Writing – review and editing

D. Frantz: Conceptualization, Funding acquisition, Methodology, Resources, Supervision

Tables and Figures

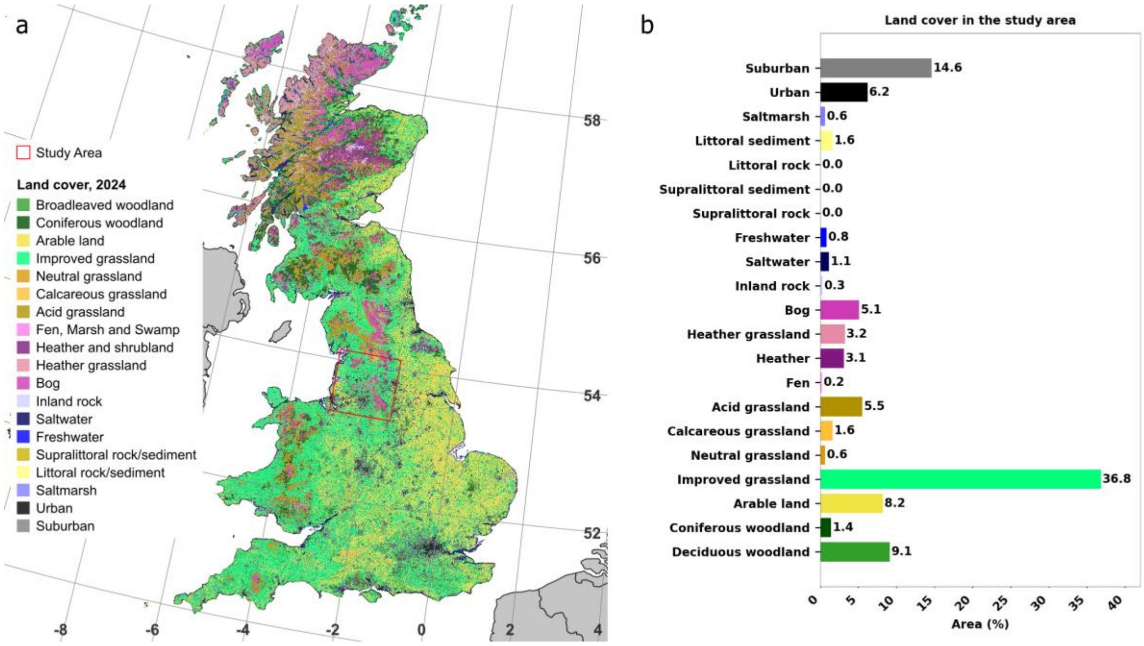

Figure 1 Study area: Military Grid Reference System tile 30UWE. Land cover representative for 2024 from Rowland et al. (2025). Country borders from www.naturalearthdata.com. CRS: EPSG 3035. b: Shares of land cover in the study area.

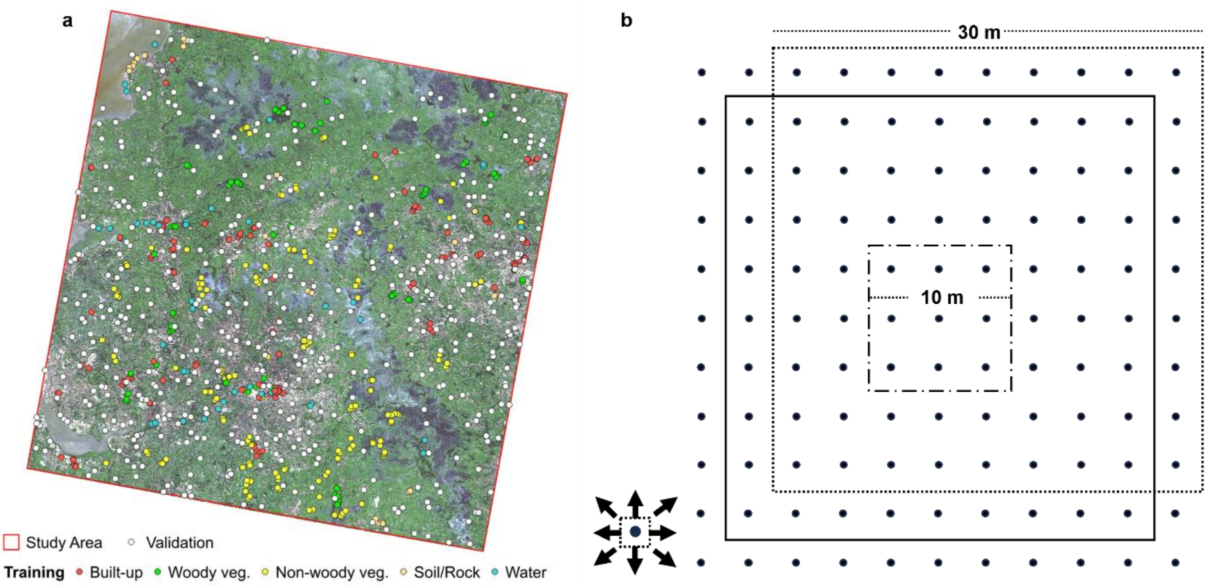

Figure 2 a) Study area including all training (n = 468) and validation (n = 450) locations. Background: Median red, green, blue reflectance of 2024 at 70% opacity. b) Validation scheme: We labeled land cover at 11 x 11 points. We compared our predicted results with the reference surface fractions of 9 x 9 points, i.e., the shares of each land surface type within 30-m of the center pixel (solid line). We also compared our maps to the reference surface fractions of 9 x 9 points when the reference is shifted by one point into each direction (Queen contiguity), accounting for potential misalignments and geolocation errors.

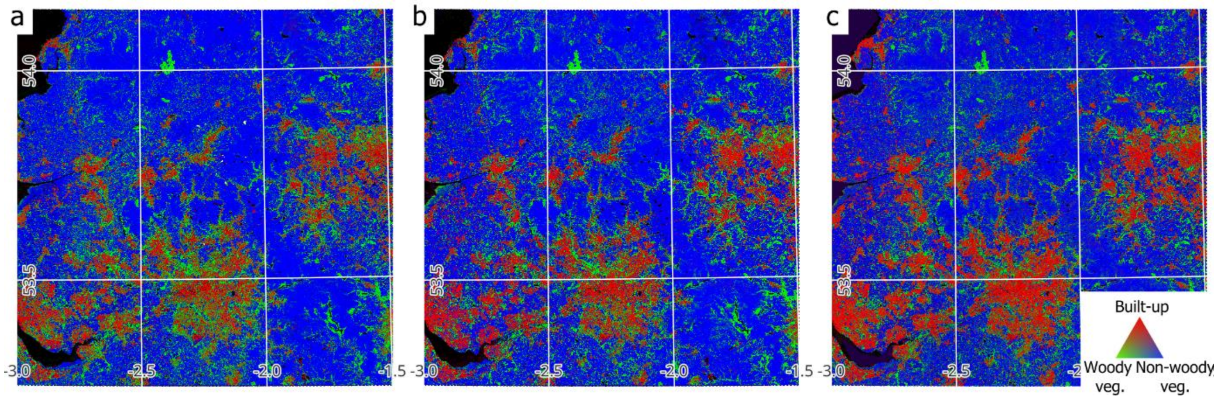

Figure 3 Predicted land cover fractions of built-up surfaces (red), woody (green) and non-woody vegetation (blue) using Sentinel-based spectral-temporal metrics (a), spline coefficients (b), and TESSERA latent embeddings (c). Model: same-year model for 2024.

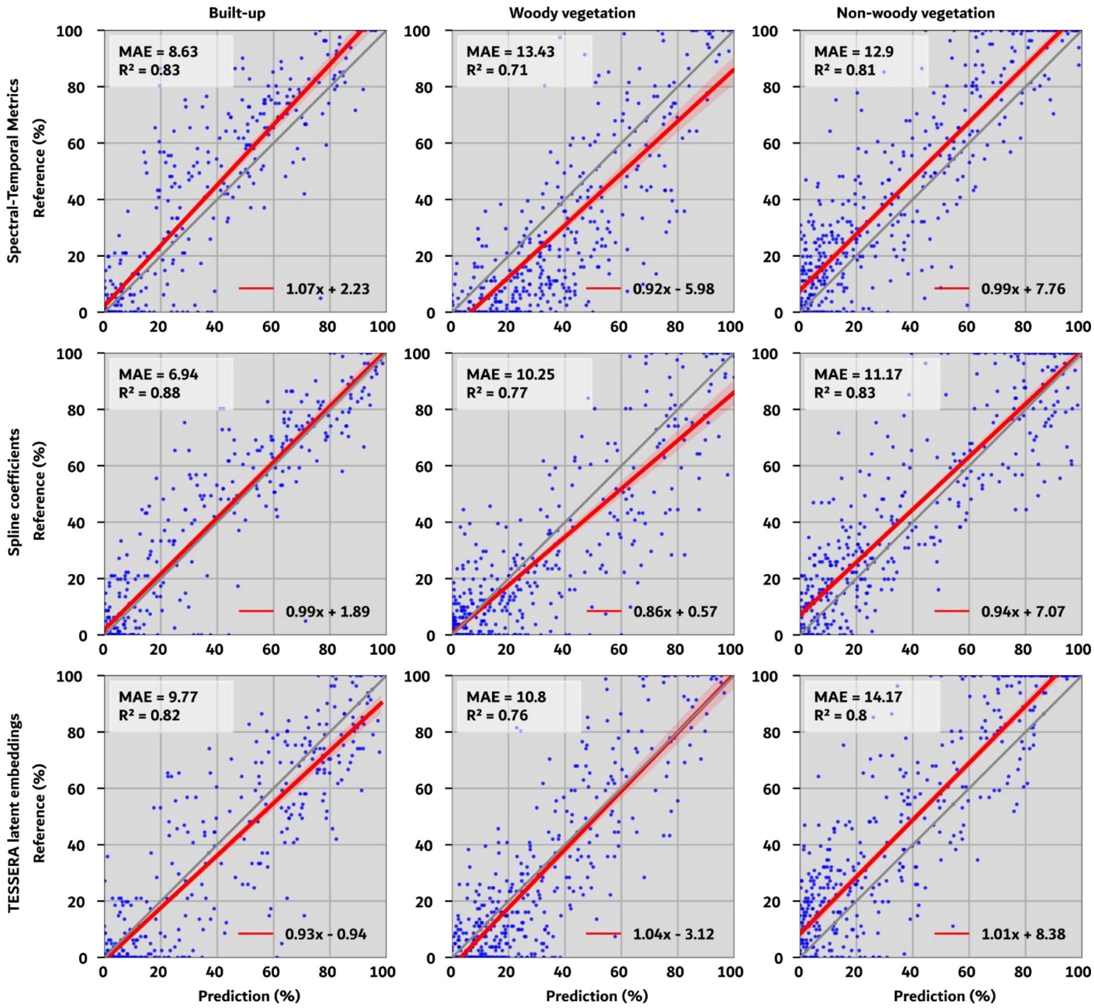

Figure 4: Performance of land cover fraction models based on spectral-temporal metrics (top), spline coefficients (center), and TESSERA latent embedding (bottom) for built-up, woody vegetation, and non-woody vegetation surfaces. Example of same-year models for 2024.

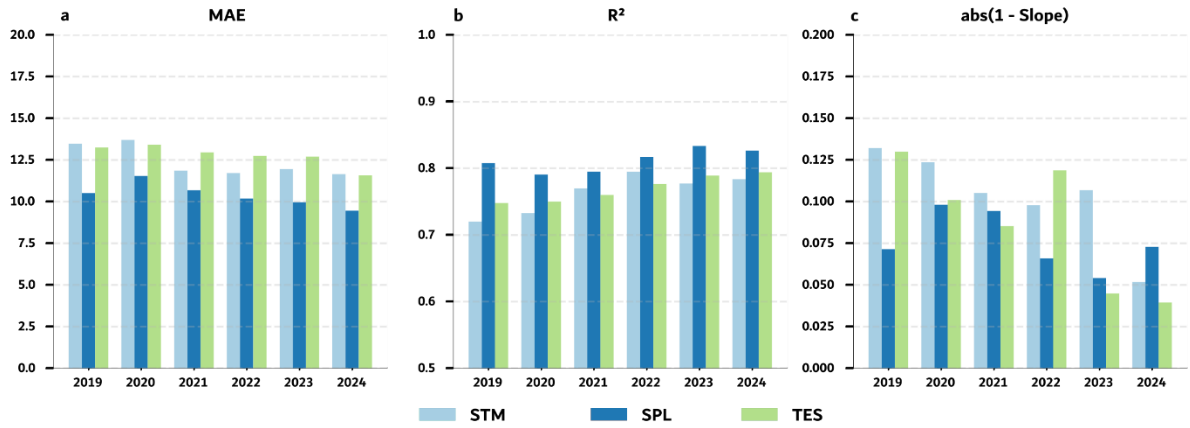

Figure 5 Mean absolute errors (a), coefficients of determination (b), and slope (c) averaged across all classes for all same-year models and all three approaches. STM: Spectral-temporal metrics, SPL: Spline coefficients, TES: TESSERA latent embeddings.

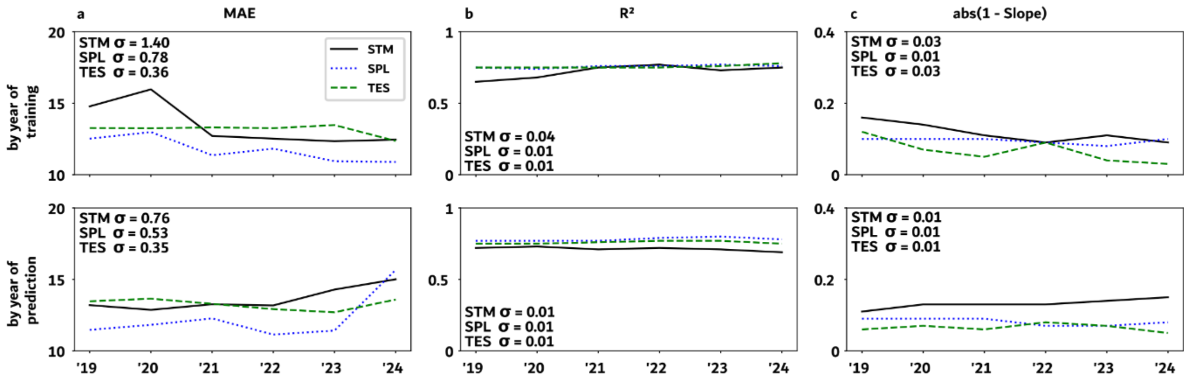

Figure 6 Mean absolute error (a), coefficient of determination (b), and Slope (c) averaged across all classes for all years, aggregated by year of training (top) and year of prediction (bottom). STM: Spectral-temporal metrics, SPL: Spline coefficients, TES: TESSERA latent embeddings, σ: Standard deviation.

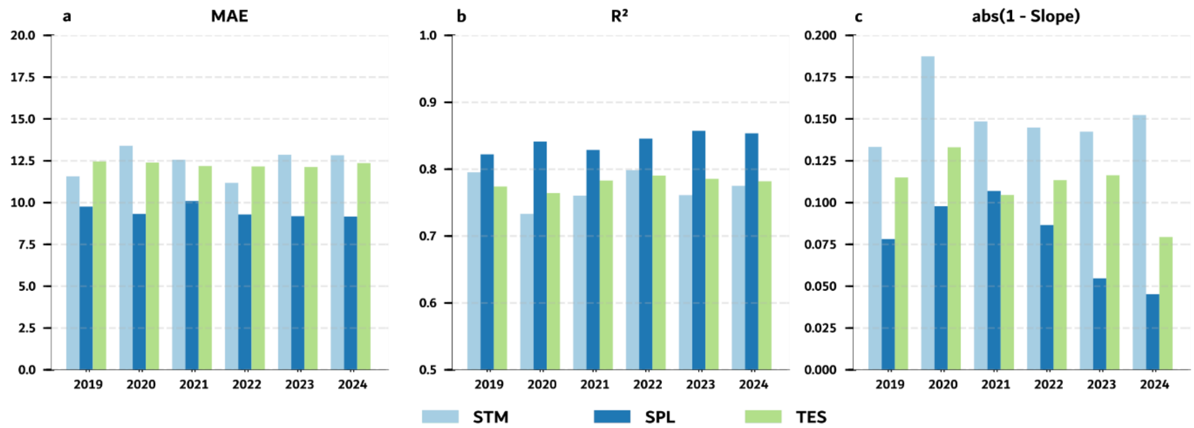

Figure 7 Mean absolute errors (a), coefficients of determination (b), and Slope (c) averaged across all classes for all temporally generalized models and all three approaches. STM: Spectral-temporal metrics, SPL: Spline coefficients, TES: TESSERA latent embeddings.

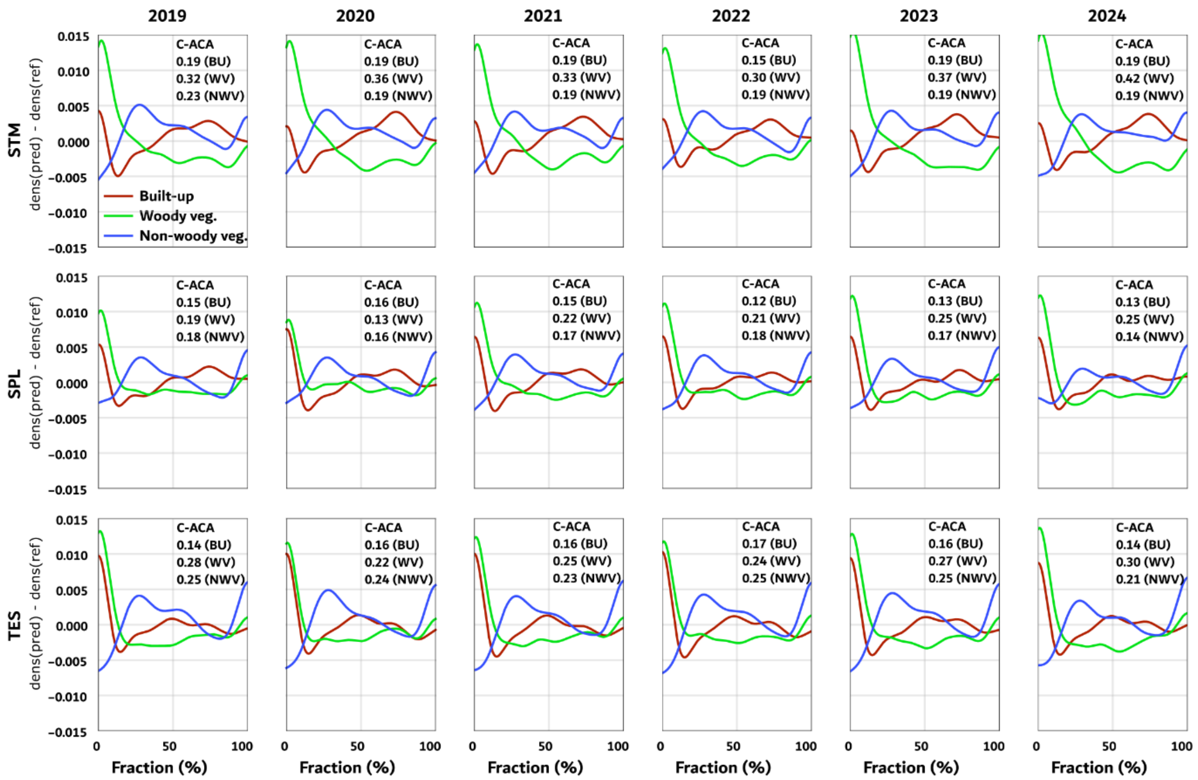

Figure 8 Difference of density plots of 1) all reference fractions in the 450 validation points and 2) the mapped fractions of the temporally generalized model in these same validation points for each class, each approach, and each year. The validation points were considered temporally invariant, which is why the difference to the distribution of mapped fractions was considered an error, and any changes in that difference across the years were considered an effect of model performance. Thus, a consistent area under the curve indicates a temporally consistent model performance. STM: Spectral-temporal metrics, SPL: Spline coefficients, TES: TESSERA latent embeddings, C-ACA: Absolute cumulative area between curve and axis. The lower the C-ACA, the closer the distribution of predictions is to the distribution of reference fractions. The more consistent the C-ACA is across years, the more consistent are the model predictions given that the references are assumed to be temporarily invariant.

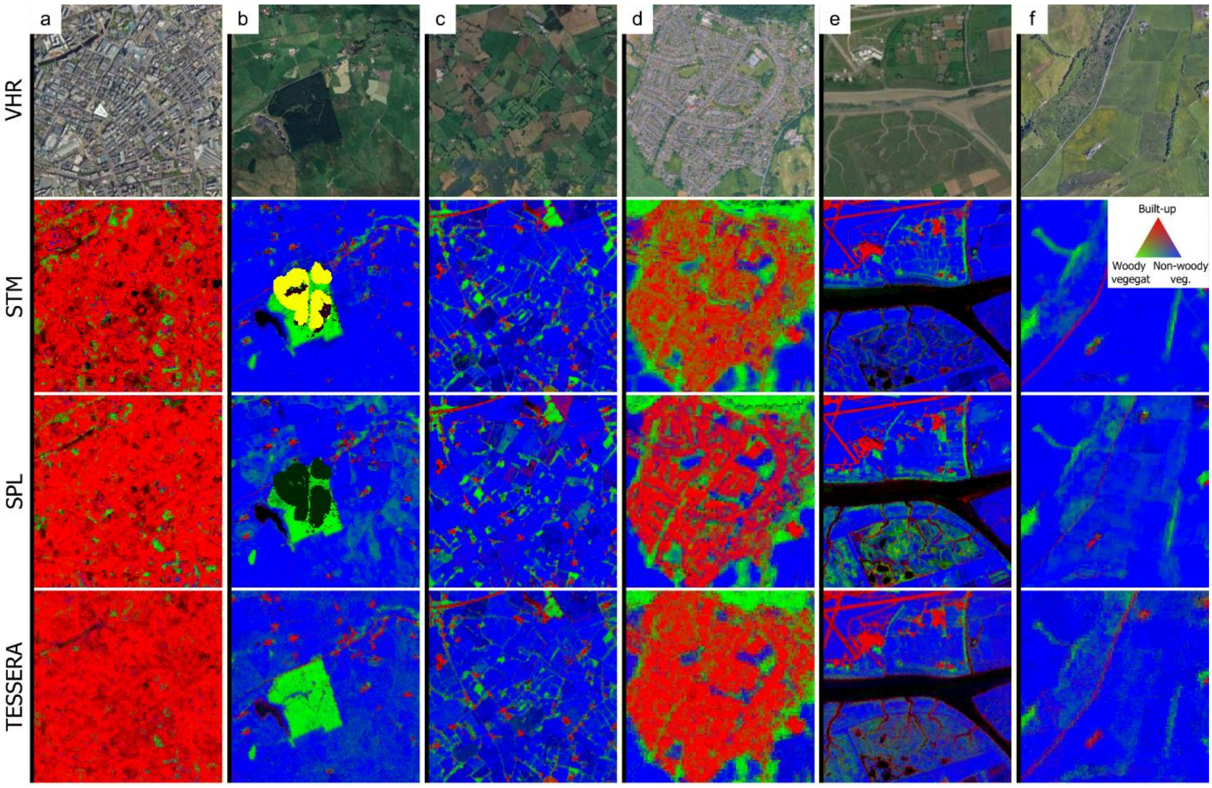

Figure 9 Examples of land cover fraction maps of built-up surfaces (red), woody-vegetation (green), and non-woody vegetation (blue) across the study area in urban, suburban, forested, managed agriculture and grassland, and wetlands. Yellow: No data.

Table 2 Number of locations for training data sampling per sampling class and associated target class.

Target Class	Sampling Class	Locations
Impervious surface	Building	66
	Road and rail	69
Woody vegetation	Deciduous woodland	47
	Coniferous woodland	31
Non-Woody Vegetation	Arable land	52
	Improved grassland	45
	Other grassland	33
	Bog, fen, and marsh vegetation	52
Soil and Rock		30
Water		43
Total		468

Table 3 Class-wise mean and standard deviation of cumulative areas between the curves and axes across all years and approaches for temporally generalized models. Cumulative area between the curve and axis describes the difference between the density plots of 1) all reference fractions in the 450 validation points and 2) the mapped fractions of the temporally generalized model in these same validation points. The lower the means, the closer the distribution of predictions is to the distribution of reference fractions. The lower the standard deviations, the more consistent are the model predictions given that the references are assumed to be temporarily invariant. **Bold**: Best result per class. STM: Spectral-temporal metrics, SPL: Spline coefficients, TES: TESSERA latent embeddings

	Mean			Standard deviation		
Class	**STM**	**SPL**	**TES**	**STM**	**SPL**	**TES**
BU	0.183	**0.140**	0.156	0.012	0.015	**0.011**
WV	0.349	**0.210**	0.262	0.039	0.041	**0.029**
NWV	0.197	**0.166**	0.236	0.013	**0.012**	**0.012**

References

Adams, J. B.; Smith, M. O.; Johnson, P. E. (1986): Spectral mixture modeling: A new analysis of rock and soil types at the Viking Lander 1 Site. In *Journal of Geophysical Research: Atmospheres* 91 (B8), p. 8098. DOI: 10.1029/JB091iB08p08098.

Azzari, G.; Lobell, D. B. (2017): Landsat-based classification in the cloud: An opportunity for a paradigm shift in land cover monitoring. In *Remote Sensing of Environment* 202, pp. 64–74. DOI: 10.1016/j.rse.2017.05.025.

Bolton, D. K.; Gray, J. M.; Melaas, E. K.; Moon, M.; Eklundh, L.; Friedl, M. A. (2020): Continental-scale land surface phenology from harmonized Landsat 8 and Sentinel-2 imagery. In *Remote Sensing of Environment* 240, p. 111685. DOI: 10.1016/j.rse.2020.111685.

Brown, C. F.; Kazmierski, M. R.; Pasquarella, V. J.; Rucklidge, W. J.; Samsikova, M.; Zhang, C. et al. (2025): AlphaEarth Foundations: An embedding field model for accurate and efficient global mapping from sparse label data. Available online at https://arxiv.org/pdf/2507.22291.

Bullock, E. L.; Woodcock, C. E.; Olofsson, P. (2020): Monitoring tropical forest degradation using spectral unmixing and Landsat time series analysis. In *Remote Sensing of Environment* 238, p. 110968. DOI: 10.1016/j.rse.2018.11.011.

Chen, S.; Woodcock, C. E.; Bullock, E. L.; Arévalo, P.; Torchinava, P.; Peng, S.; Olofsson, P. (2021): Monitoring temperate forest degradation on Google Earth Engine using Landsat time series analysis. In *Remote Sensing of Environment* 265, p. 112648. DOI: 10.1016/j.rse.2021.112648.

Drusch, M.; Del Bello, U.; Carlier, S.; Colin, O.; Fernandez, V.; Gascon, F. et al. (2012): Sentinel-2: ESA's Optical High-Resolution Mission for GMES Operational Services. In *Remote Sensing of Environment* 120, pp. 25–36. DOI: 10.1016/j.rse.2011.11.026.

Feng, Z.; Atzberger, C.; Jaffer, S.; Knezevic, J.; Sormunen, S.; Young, R. et al. (2025): TESSERA: Temporal Embeddings of Surface Spectra for Earth Representation and Analysis. Available online at https://arxiv.org/pdf/2506.20380.

Frantz, D. (2019): FORCE—Landsat + Sentinel-2 Analysis Ready Data and Beyond. In *Remote Sensing* 11 (9), p. 1124. DOI: 10.3390/rs11091124.

Frantz, D.; Haß, E.; Uhl, A.; Stoffels, J.; Hill, J. (2018): Improvement of the Fmask algorithm for Sentinel-2 images. Separating clouds from bright surfaces based on parallax effects. In *Remote Sensing of Environment* 215, pp. 471–481. DOI: 10.1016/j.rse.2018.04.046.

Frantz, D.; Röder, A.; Stellmes, M.; Hill, J. (2016a): An Operational Radiometric Landsat Preprocessing Framework for Large-Area Time Series Applications. In *IEEE Transactions on Geoscience and Remote Sensing* 54 (7), pp. 3928–3943. DOI: 10.1109/TGRS.2016.2530856.

Frantz, D.; Rufin, P.; Janz, A.; Ernst, S.; Pflugmacher, D.; Schug, F.; Hostert, P. (2023): Understanding the robustness of spectral-temporal metrics across the global Landsat archive from 1984 to 2019 – a quantitative evaluation. In *Remote Sensing of Environment* 298, p. 113823. DOI: 10.1016/j.rse.2023.113823.

Frantz, D.; Schug, F.; Okujeni, A.; Navacchi, C.; Wagner, W.; van der Linden, S.; Hostert, P. (2021): National-scale mapping of building height using Sentinel-1 and Sentinel-2 time series. In *Remote Sensing of Environment* 252, p. 112128. DOI: 10.1016/j.rse.2020.112128.

Frantz, D.; Stellmes, M.; Roder, A.; Udelhoven, T.; Mader, S.; Hill, J. (2016b): Improving the Spatial Resolution of Land Surface Phenology by Fusing Medium- and Coarse-Resolution

Inputs. In *IEEE Transactions on Geoscience and Remote Sensing* 54 (7), pp. 4153–4164. DOI: 10.1109/TGRS.2016.2537929.

Gascon, F. (2019): Sentinel-2 Mission Status. ESA. Frascati, IT, 2019.

Gullì, A.; Pal, S. (2017): Deep learning with Keras. Implement neural networks with Keras on Theano and TensorFlow. Birmingham: Packt Publishing. 978-1787128422.

Guzha, A. C.; Rufino, M. C.; Okoth, S.; Jacobs, S.; Nóbrega, R. (2018): Impacts of land use and land cover change on surface runoff, discharge and low flows: Evidence from East Africa. In *Journal of Hydrology: Regional Studies* 15, pp. 49–67. DOI: 10.1016/j.ejrh.2017.11.005.

Hansen, M. C.; Potapov, P. V.; Moore, R.; Hancher, M.; Turubanova, S. A.; Tyukavina, A. et al. (2013): High-resolution global maps of 21st-century forest cover change. In *Science* 342 (6160), pp. 850–853. DOI: 10.1126/science.1244693.

Harkort, L.; Okujeni, A.; Amputu, V.; Mahler, J.; Nill, L.; Pflugmacher, D. et al. (2025): Mapping fractional vegetation cover in Sub-Saharan rangelands using phenological feature spaces. In *Remote Sensing of Environment* 319, p. 114646. DOI: 10.1016/j.rse.2025.114646.

Huang, Z.; Yan, H.; Zhan, Q.; Yang, S.; Zhang, M.; Zhang, C. et al. (2025): A Survey on Remote Sensing Foundation Models: From Vision to Multimodality. DOI: 10.48550/arXiv.2503.22081.

Jackson, H. Bird; Fahrig, L. (2015): Are ecologists conducting research at the optimal scale? In *Global Ecology and Biogeography* 24 (1), pp. 52–63. DOI: 10.1111/geb.12233.

Jilge, M.; Heiden, U.; Habermeyer, M.; Mende, A.; Juergens, C. (2017): Detecting Unknown Artificial Urban Surface Materials Based on Spectral Dissimilarity Analysis. In *Sensors* 17 (8). DOI: 10.3390/s17081826.

Jones, M. O.; Allred, B. W.; Naugle, D. E.; Maestas, J. D.; Donnelly, P.; Metz, L. J. et al. (2018): Innovation in rangeland monitoring: annual, 30 m, plant functional type percent cover maps for U.S. rangelands, 1984–2017. In *Ecosphere* 9 (9), Article e02430. DOI: 10.1002/ecs2.2430.

Kauth, R. J.; Thomas, G. S. (1976): The Tasseled Cap - a graphic description of the spectral-temporal development of agricultural crops as seen by Landsat. In : Proceedings of the Symposium on Machine Processing of Remotely Sensed Data. Purdue University, 4B31 - 4B51.

Kingma, D. P.; Ba, J. (2014): Adam: A Method for Stochastic Optimization. In *arXiv*. DOI: 10.48550/arXiv.1412.6980.

Klehr, D.; Stoffels, J.; Hill, A.; Pham, V.-D.; van der Linden, S.; Frantz, D. (2025): Mapping tree species fractions in temperate mixed forests using Sentinel-2 time series and synthetically mixed training data. In *Remote Sensing of Environment* 323, p. 114740. DOI: 10.1016/j.rse.2025.114740.

Kowalski, K.; Okujeni, A.; Hostert, P. (2023): A generalized framework for drought monitoring across Central European grassland gradients with Sentinel-2 time series. In *Remote Sensing of Environment* 286, p. 113449. DOI: 10.1016/j.rse.2022.113449.

LaFontaine, J. H.; Hay, L. E.; Viger, R. J.; Regan, R. Steve; Markstrom, S. L. (2015): Effects of Climate and Land Cover on Hydrology in the Southeastern U.S.: Potential Impacts on Watershed Planning. In *JAWRA Journal of the American Water Resources Association* 51 (5), pp. 1235–1261. DOI: 10.1111/1752-1688.12304.

Lewińska, K. E.; Buchner, J.; Bleyhl, B.; Hostert, P.; Yin, H.; Kuemmerle, T.; Radeloff, V. C. (2021): Changes in the grasslands of the Caucasus based on Cumulative Endmember Fractions from the full 1987–2019 Landsat record. In *Science of Remote Sensing* 4, p. 100035. DOI: 10.1016/j.srs.2021.100035.

Lewińska, K. E.; Ernst, S.; Frantz, D.; Leser, U.; Hostert, P. (2024): Global overview of usable Landsat and Sentinel-2 data for 1982-2023. In *Data in brief* 57, p. 111054. DOI: 10.1016/j.dib.2024.111054.

Lewińska, K. E.; Hostert, P.; Buchner, J.; Bleyhl, B.; Radeloff, V. C. (2020): Short-term vegetation loss versus decadal degradation of grasslands in the Caucasus based on Cumulative Endmember Fractions. In *Remote Sensing of Environment* 248, p. 111969. DOI: 10.1016/j.rse.2020.111969.

Lewińska, K. E; Okujeni, A.; Kowalski, K.; Lehmann, F.; Radeloff, V. C.; Leser, U.; Hostert, P. (2025): Impact of data density and endmember definitions on long-term trends in ground cover fractions across European grasslands. In *Remote Sensing of Environment* 323, p. 114736. DOI: 10.1016/j.rse.2025.114736.

Lobert, F.; Schwieder, M.; Alsleben, J.; Broeg, T.; Kowalski, K.; Okujeni, A. et al. (2025): Unveiling year-round cropland cover by soil-specific spectral unmixing of Landsat and Sentinel-2 time series. In *Remote Sensing of Environment* 318, p. 114594. DOI: 10.1016/j.rse.2024.114594.

Mai, G.; Huang, W.; Sun, J.; Song, S.; Mishra, D.; Liu, N. et al. (2023): On the Opportunities and Challenges of Foundation Models for Geospatial Artificial Intelligence. Available online at http://arxiv.org/pdf/2304.06798v1.

Marconcini, M.; Metz-Marconcini, A.; Esch, T.; Gorelick, N. (2021): Understanding Current Trends in Global Urbanisation - The World Settlement Footprint Suite. In *GI_Forum* 1, pp. 33–38. DOI: 10.1553/giscience2021_01_s33.

Montero, A.; Marull, J.; Tello, E.; Cattaneo, C.; Coll, F.; Pons, M. et al. (2021): The impacts of agricultural and urban land-use changes on plant and bird biodiversity in Costa Rica (1986–2014). In *Regional Environmental Change* 21 (2). DOI: 10.1007/s10113-021-01767-1.

Nill, L.; Grünberg, I.; Ullmann, T.; Gessner, M.; Boike, J.; Hostert, P. (2022): Arctic shrub expansion revealed by Landsat-derived multitemporal vegetation cover fractions in the Western Canadian Arctic. In *Remote Sensing of Environment* 281, p. 113228. DOI: 10.1016/j.rse.2022.113228.

Okujeni, A.; Kowalski, K.; Lewińska, K. E.; Schneidereit, S.; Hostert, P. (2024): Multidecadal grassland fractional cover time series retrieval for Germany from the Landsat and Sentinel-2 archives. In *Remote Sensing of Environment* 302, p. 113980. DOI: 10.1016/j.rse.2023.113980.

Okujeni, A.; van der Linden, S.; Suess, S.; Hostert, P. (2017): Ensemble Learning From Synthetically Mixed Training Data for Quantifying Urban Land Cover With Support Vector Regression. In *IEEE Journal of Selected Topics in Applied Earth Observations and Remote Sensing* 10 (4), pp. 1640–1650. DOI: 10.1109/JSTARS.2016.2634859.

Okujeni, A.; van der Linden, S.; Tits, L.; Somers, B.; Hostert, P. (2013): Support vector regression and synthetically mixed training data for quantifying urban land cover. In *Remote Sensing of Environment* 137, pp. 184–197. DOI: 10.1016/j.rse.2013.06.007.

Pesaresi, M.; Schiavina, M.; Politis, P.; Freire, S.; Krasnodębska, K.; Uhl, J. H. et al. (2024): Advances on the Global Human Settlement Layer by joint assessment of Earth Observation and population survey data. In *International Journal of Digital Earth* 17 (1), Article 2390454. DOI: 10.1080/17538947.2024.2390454.

Pflugmacher, D.; Rabe, A.; Peters, M.; Hostert, P. (2019): Mapping pan-European land cover using Landsat spectral-temporal metrics and the European LUCAS survey. In *Remote Sensing of Environment* 221, pp. 583–595. DOI: 10.1016/j.rse.2018.12.001.

Pfoch, K. A.; Schug, F.; Cox, H. R.; Pham, V.-D.; van der Linden, S.; Radeloff, V. C. (2026): Monitoring growth of the wildland-urban interface in 2000 and 2020 in Mediterranean ecosystems with Landsat satellite imagery. In *Science of Remote Sensing* 13, p. 100387. DOI: 10.1016/j.srs.2026.100387.

Phalke, A. R.; Özdoğan, M. (2018): Large area cropland extent mapping with Landsat data and a generalized classifier. In *Remote Sensing of Environment* 219, pp. 180–195. DOI: 10.1016/j.rse.2018.09.025.

Pham, V.-D.; Thiel, F.; Frantz, D.; Okujeni, A.; Schug, F.; van der Linden, S. (2024): Learning the variations in annual spectral-temporal metrics to enhance the transferability of regression models for land cover fraction monitoring. In *Remote Sensing of Environment* 308, p. 114206. DOI: 10.1016/j.rse.2024.114206.

Phinn, S.; Stanford, M.; Scarth, P.; Murray, A. T.; Shyy, P. T. (2002): Monitoring the composition of urban environments based on the vegetation-impervious surface-soil (VIS) model by subpixel analysis techniques. In *International Journal of Remote Sensing* 23 (20), pp. 4131–4153. DOI: 10.1080/01431160110114998.

Potapov, P.; Turubanova, S.; Hansen, M. C.; Tyukavina, A.; Zalles, V.; Khan, A. et al. (2022): Global maps of cropland extent and change show accelerated cropland expansion in the twenty-first century. In *Nature Food* 3 (1), pp. 19–28. DOI: 10.1038/s43016-021-00429-z.

Potapov, P. V.; Turubanova, S. A.; Tyukavina, A.; Krylov, A. M.; McCarty, J. L.; Radeloff, V. C.; Hansen, M. C. (2015): Eastern Europe's forest cover dynamics from 1985 to 2012 quantified from the full Landsat archive. In *Remote Sensing of Environment* 159, pp. 28–43. DOI: 10.1016/j.rse.2014.11.027.

Priem, F.; Jilge, M.; Heiden, U.; Somers, B.; Canters, F. (2025): Generic spectral library framework for urban land cover mapping with optical remote sensing imagery. In *Environmental Modelling & Software* 188, p. 106405. DOI: 10.1016/j.envsoft.2025.106405.

Radeloff, V. C.; Mockrin, M. H.; Helmers, D.; Carlson, A.; Hawbaker, T. J.; Martinuzzi, S. et al. (2023): Rising wildfire risk to houses in the United States, especially in grasslands and shrublands. In *Science* 382 (6671), pp. 702–707. DOI: 10.1126/science.ade9223.

Ridd, M. K. (1995): Exploring a V-I-S (vegetation-impervious surface-soil) model for urban ecosystem analysis through remote sensing. Comparative anatomy for cities. In *International Journal of Remote Sensing* 16 (12), pp. 2165–2185. DOI: 10.1080/01431169508954549.

Rioux, J.-F.; Cimon-Morin, J.; Pellerin, S.; Alard, D.; Poulin, M. (2019): How Land Cover Spatial Resolution Affects Mapping of Urban Ecosystem Service Flows. In *Frontiers in Environmental Science* 7, Article 93. DOI: 10.3389/fenvs.2019.00093.

Roberts, D. A.; Gardner, M.; Church, R.; Ustin, S.; Scheer, G.; Green, R. O. (1998): Mapping Chaparral in the Santa Monica Mountains Using Multiple Endmember Spectral Mixture Models. In *Remote Sensing of Environment* 65 (3), pp. 267–279. DOI: 10.1016/S0034-4257(98)00037-6.

Rowland, C. S.; Marston, C. G.; O'Neil, A. W. (2025): Land Cover Map 2024 (10m classified pixels, GB). With assistance of C. G. Marston, UK Centre for Ecology & Hydrology, NERC EDS Environmental Information Data Centre.

Schug, F.; Frantz, D.; Okujeni, A.; van der Linden, S.; Hostert, P. (2020): Mapping urban-rural gradients of settlements and vegetation at national scale using Sentinel-2 spectral-temporal metrics and regression-based unmixing with synthetic training data. In *Remote Sensing of Environment* 246, p. 111810. DOI: 10.1016/j.rse.2020.111810.

Schug, F.; Pfoch, K.; Pham, V.-D.; van der Linden, S.; Okujeni, A.; Frantz, D.; Radeloff, V. C. (2024): Land cover fraction mapping across global biomes with Landsat data, spatially generalized regression models and spectral-temporal metrics. In *Remote Sensing of Environment* 311, p. 114260. DOI: 10.1016/j.rse.2024.114260.

Senf, C.; Laštovička, J.; Okujeni, A.; Heurich, M.; van der Linden, S. (2020): A generalized regression-based unmixing model for mapping forest cover fractions throughout three decades of Landsat data. In *Remote Sensing of Environment* 240, p. 111691. DOI: 10.1016/j.rse.2020.111691.

Senf, C.; Seidl, R. (2021): Mapping the forest disturbance regimes of Europe. In *Nature Sustainability* 4 (1), pp. 63–70. DOI: 10.1038/s41893-020-00609-y.

Shao, M.; Zhao, G.; Kao, S.-C.; Cuo, L.; Rankin, C.; Gao, H. (2020): Quantifying the effects of urbanization on floods in a changing environment to promote water security — A case study of two adjacent basins in Texas. In *Journal of Hydrology* 589, p. 125154. DOI: 10.1016/j.jhydrol.2020.125154.

Simkin, R. D.; Seto, K. C.; McDonald, R. I.; Jetz, W. (2022): Biodiversity impacts and conservation implications of urban land expansion projected to 2050. In *Proceedings of the National Academy of Sciences of the United States of America* 119 (12), e2117297119. DOI: 10.1073/pnas.2117297119.

Small, C. (2004): The Landsat ETM+ spectral mixing space. In *Remote Sensing of Environment* 93 (1-2), pp. 1–17. DOI: 10.1016/j.rse.2004.06.007.

Small, C.; Milesi, C. (2013): Multi-scale standardized spectral mixture models. In *Remote Sensing of Environment* 136, pp. 442–454. DOI: 10.1016/j.rse.2013.05.024.

Small, C.; Sousa, D. (2022): The Sentinel 2 MSI Spectral Mixing Space. In *Remote Sensing* 14 (22), p. 5748. DOI: 10.3390/rs14225748.

Small, C.; Sousa, D. (2023): Spectral Characteristics of the Dynamic World Land Cover Classification. In *Remote Sensing* 15 (3), p. 575. DOI: 10.3390/rs15030575.

Small, D. (2012): SAR backscatter multitemporal compositing via local resolution weighting. In : 2012 IEEE International Geoscience and Remote Sensing Symposium. IGARSS 2012 - 2012 IEEE International Geoscience and Remote Sensing Symposium. Munich, Germany, 2012: IEEE, pp. 4521–4524.

Smith, M. O.; Ustin, S. L.; Adams, J. B.; Gillespie, A. R. (1990): Vegetation in deserts: I. A regional measure of abundance from multispectral images. In *Remote Sensing of Environment* 31 (1), pp. 1–26. DOI: 10.1016/0034-4257(90)90074-V.

Sousa, D.; Davis, F. W. (2020): Scalable mapping and monitoring of Mediterranean-climate oak landscapes with temporal mixture models. In *Remote Sensing of Environment* 247, p. 111937. DOI: 10.1016/j.rse.2020.111937.

Sousa, D.; Small, C. (2019): Globally standardized MODIS spectral mixture models. In *Remote Sensing Letters* 10 (10), pp. 1018–1027. DOI: 10.1080/2150704X.2019.1634299.

Stanimirova, R.; Graesser, J.; Olofsson, P.; Friedl, M. A. (2022): Widespread changes in 21st century vegetation cover in Argentina, Paraguay, and Uruguay. In *Remote Sensing of Environment* 282, p. 113277. DOI: 10.1016/j.rse.2022.113277.

Suess, S.; van der Linden, S.; Okujeni, A.; Griffiths, P.; Leitão, P. J.; Schwieder, M.; Hostert, P. (2018): Characterizing 32 years of shrub cover dynamics in southern Portugal using annual Landsat composites and machine learning regression modeling. In *Remote Sensing of Environment* 219, pp. 353–364. DOI: 10.1016/j.rse.2018.10.004.

Szwarcman, D.; Roy, S.; Fraccaro, P.; Gíslason, Þ. Elí; Blumenstiel, B.; Ghosal, R. et al. (2024): Prithvi-EO-2.0: A Versatile Multi-Temporal Foundation Model for Earth Observation Applications. Available online at https://arxiv.org/pdf/2412.02732.

Timoner, P.; Poussin, C.; Planque, C.; Lucas, R. M.; Feng, Z.; Lambiel, A. et al. (2026): Exploring the potential of geo-embeddings to produce relevant environmental descriptors for land cover mapping.

Tseng, G.; Cartuyvels, R.; Zvonkov, I.; Purohit, M.; Rolnick, D.; Kerner, H. (2023): Lightweight, Pre-trained Transformers for Remote Sensing Timeseries. Available online at https://arxiv.org/pdf/2304.14065.

Tucker, C. J. (1979): Red and photographic infrared linear combinations for monitoring vegetation. In *Remote Sensing of Environment* 8 (2), pp. 127–150. DOI: 10.1016/0034-4257(79)90013-0.

van der Linden, S.; Okujeni, A.; Canters, F.; Degerickx, J.; Heiden, U.; Hostert, P. et al. (2018): Imaging Spectroscopy of Urban Environments. In *Surveys in Geophysics* 80, p. 21. DOI: 10.1007/s10712-018-9486-y.

Venter, Z. S.; Barton, D. N.; Chakraborty, T.; Simensen, T.; Singh, G. (2022): Global 10 m Land Use Land Cover Datasets: A Comparison of Dynamic World, World Cover and Esri Land Cover. In *Remote Sensing* 14 (16), p. 4101. DOI: 10.3390/rs14164101.

Viana-Soto, A.; Okujeni, A.; Pflugmacher, D.; García, M.; Aguado, I.; Hostert, P. (2022): Quantifying post-fire shifts in woody-vegetation cover composition in Mediterranean pine forests using Landsat time series and regression-based unmixing. In *Remote Sensing of Environment* 281, p. 113239. DOI: 10.1016/j.rse.2022.113239.

Vogeler, J. C.; Braaten, J. D.; Slesak, R. A.; Falkowski, M. J. (2018): Extracting the full value of the Landsat archive: Inter-sensor harmonization for the mapping of Minnesota forest canopy cover (1973–2015). In *Remote Sensing of Environment* 209, pp. 363–374. DOI: 10.1016/j.rse.2018.02.046.

Wetherley, E. B.; Roberts, D. A.; McFadden, J. P. (2017): Mapping spectrally similar urban materials at sub-pixel scales. In *Remote Sensing of Environment* 195, pp. 170–183. DOI: 10.1016/j.rse.2017.04.013.

Woodcock, C. E.; Macomber, S. A.; Pax-Lenney, M.; Cohen, W. B. (2001): Monitoring large areas for forest change using Landsat: Generalization across space, time and Landsat sensors. In *Remote Sensing of Environment* 78 (1-2), pp. 194–203. DOI: 10.1016/S0034-4257(01)00259-0.

Wulder, M. A.; Roy, D. P.; Radeloff, V. C.; Loveland, T. R.; Anderson, M. C.; Johnson, D. M. et al. (2022): Fifty years of Landsat science and impacts. In *Remote Sensing of Environment* 280, p. 113195. DOI: 10.1016/j.rse.2022.113195.

Wulder, M. A.; White, J. C.; Loveland, T. R.; Woodcock, C. E.; Belward, A. S.; Cohen, W. B. et al. (2016): The global Landsat archive: Status, consolidation, and direction. In *Remote Sensing of Environment* 185, pp. 271–283. DOI: 10.1016/j.rse.2015.11.032.

Xiao, A.; Xuan, W.; Wang, J.; Huang, J.; Tao, D.; Lu, S.; Yokoya, N. (2025): Foundation Models for Remote Sensing and Earth Observation: A survey. In *IEEE Geoscience and Remote Sensing Magazine* 13 (4), pp. 297–324. DOI: 10.1109/MGRS.2025.3576766.

Xu, P.; Tsendbazar, N.-E.; Herold, M.; Bruin, S. de; Koopmans, M.; Birch, T. et al. (2024): Comparative validation of recent 10 m-resolution global land cover maps. In *Remote Sensing of Environment* 311, p. 114316. DOI: 10.1016/j.rse.2024.114316.

Yang, L.; Chen, N.; Yue, J.; Liu, Y.; Ma, J.; Ghamisi, P. et al. (2025): Survey of Multimodal Geospatial Foundation Models: Techniques, Applications, and Challenges. Available online at https://arxiv.org/pdf/2510.22964.

Zbontar, J.; Jing, L.; Misra, I.; LeCun, Y.; Deny, S. (2021): Barlow Twins: Self-Supervised Learning via Redundancy Reduction.

Zhang, Y.; Woodcock, C. E.; Arévalo, P.; Olofsson, P.; Tang, X.; Stanimirova, R. et al. (2022): A Global Analysis of the Spatial and Temporal Variability of Usable Landsat Observations at the Pixel Scale. In *Frontiers in Remote Sensing* 3, Article 894618. DOI: 10.3389/frsen.2022.894618.

Supplementary Information for

Multi-annual sub-pixel land cover mapping with TESSERA latent embeddings

Franz Schug*, David Klehr, Jari Mahler, David Frantz

* Corresponding author: franz.schug@uni-trier.de

1. High-quality clear-sky observations

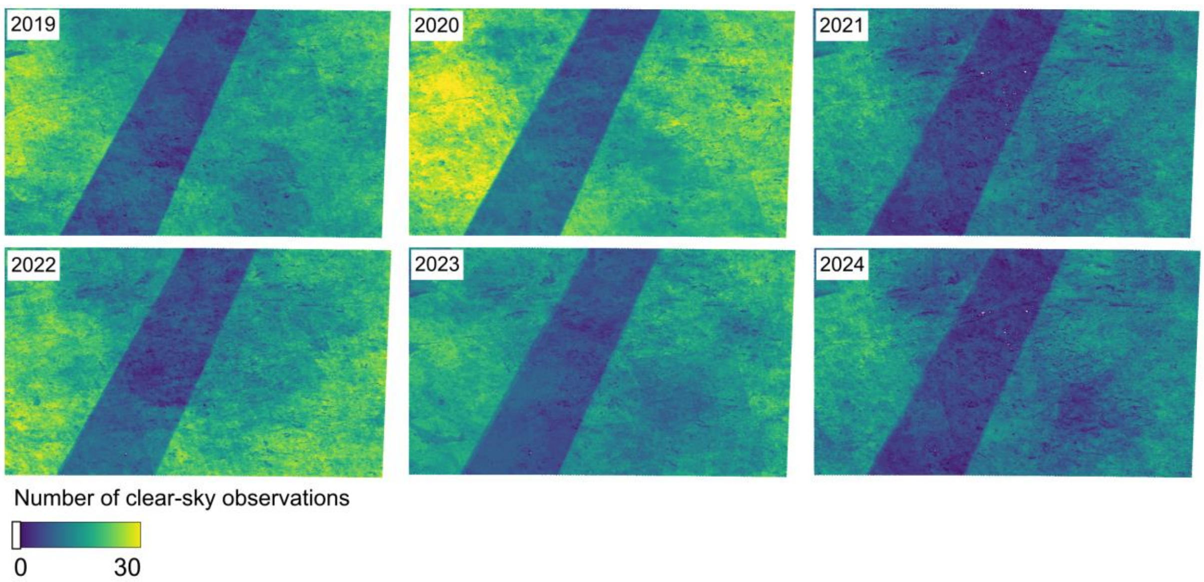

Figure-SI 1 Number of clear sky observations per pixel in our study area. Median ranges from 7 in 2024 to 12 in 2020.

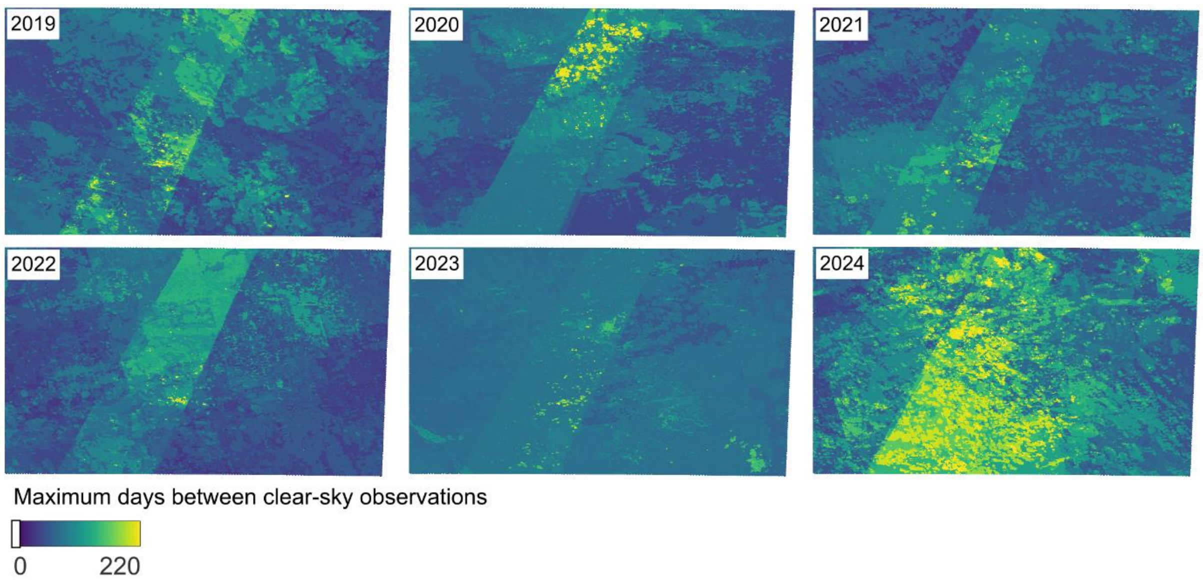

Figure-SI 2 Maximum days between clear sky observations per pixel in the study area. Median ranges from 85 days in 2023 to 155 days in 2024.

Table-SI 1 Median and 90th quantile of the number of high-quality clear-sky observations (CSO) in the study area per year, as well as the median maximum distance between high-quality clear-sky observations in days.

Year	Median CSO	Q90 CSO	Median max. distance between CSO (days)
2019	10	20	102
2020	12	25	97
2021	10	20	95
2022	10	22	100
2023	9	18	85
2024	7	16	155

2. Training data

The 21 classes provided in the UK Center for Ecology & Hydrology (UKCEH) for 2024 were condensed into ten classes that are visually identifiable using aerial or satellite data. Training locations were samples in these ten classes and then merged into our five target classes.

Table-SI 2 The 21 classes as defined by Rowland et al. (2025), the coverage of each class within our study area, the ten aggregated classes based on our own aggregation scheme, and our five target classes.

Class	UKCEH land cover	Coverage (%)	Sampling Class	Target class
1	Deciduous woodland	9.1	Deciduous woodland	Woody vegetation
2	Coniferous woodland	1.4	Coniferous woodland	
3	Arable land	8.2	Arable land	Non-woody vegetation
4	Improved grassland	36.8	Improved grassland	
5	Neutral grassland	0.6	Other grassland	
6	Calcareous grassland	1.6		
7	Acid grassland	5.5		
8	Fen	0.2	Bog, fen, and marsh	
9	Heather	3.1		
10	Heather grassland	3.2		
11	Bog	5.1		
12	Inland rock	0.3	Soil and rock	Bare soil
13	Saltwater	1.1	Water	Water
14	Freshwater	0.8		
15	Supralittoral rock	0.0	Soil and rock	Bare soil
16	Supralittoral sediment	0.0		
17	Littoral rock	0.0		
18	Littoral sediment	1.6		
19	Saltmarsh	0.6	Bog, fen, and marsh	Non-woody vegetation
20	Urban	6.2	Building	Built-up
21	Suburban	14.6	Other built-up	

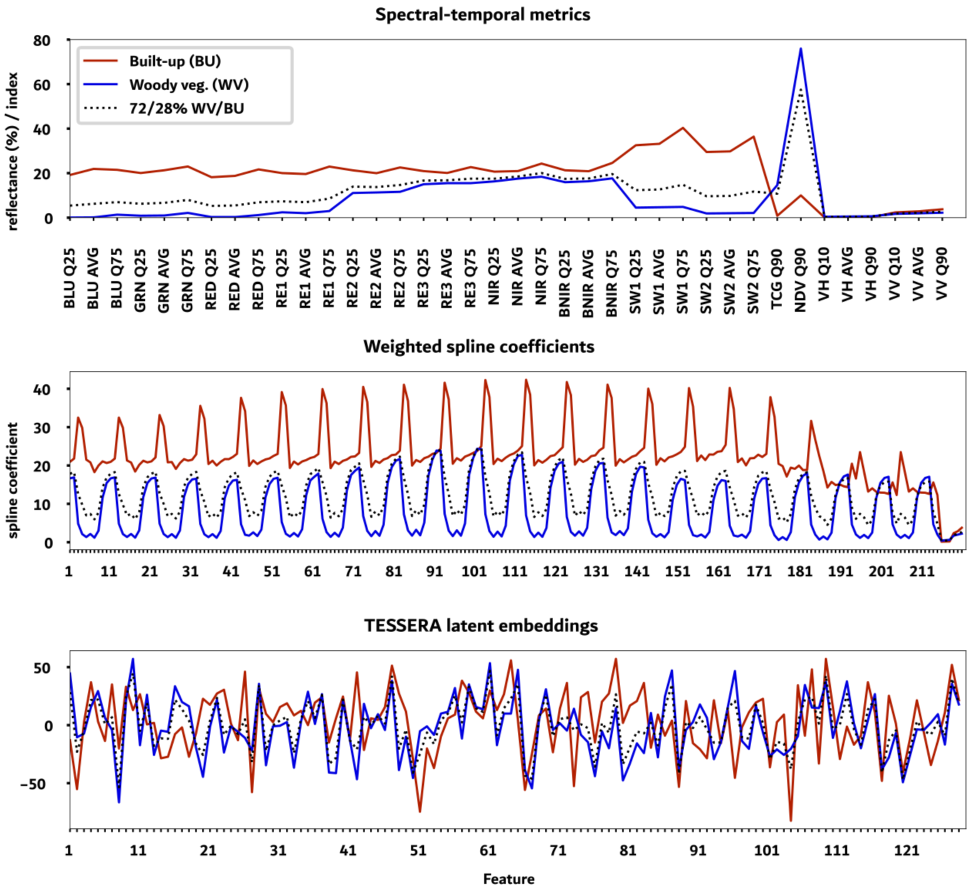

Figure-SI 3 Examples of signatures for training regression models for built-up surface and woody vegetation fractions based on spectral-temporal metrics (*top*), weighted spline coefficients (*center*), and TESSERA latent embeddings (*bottom*). Red and blue correspond to a *pure* surface. The dashed black line corresponds to a synthetic linear mixture that would be used for training a regression model for built-up surfaces (with 28% as label) and woody vegetation (with 72% as label).

3. Extended validation

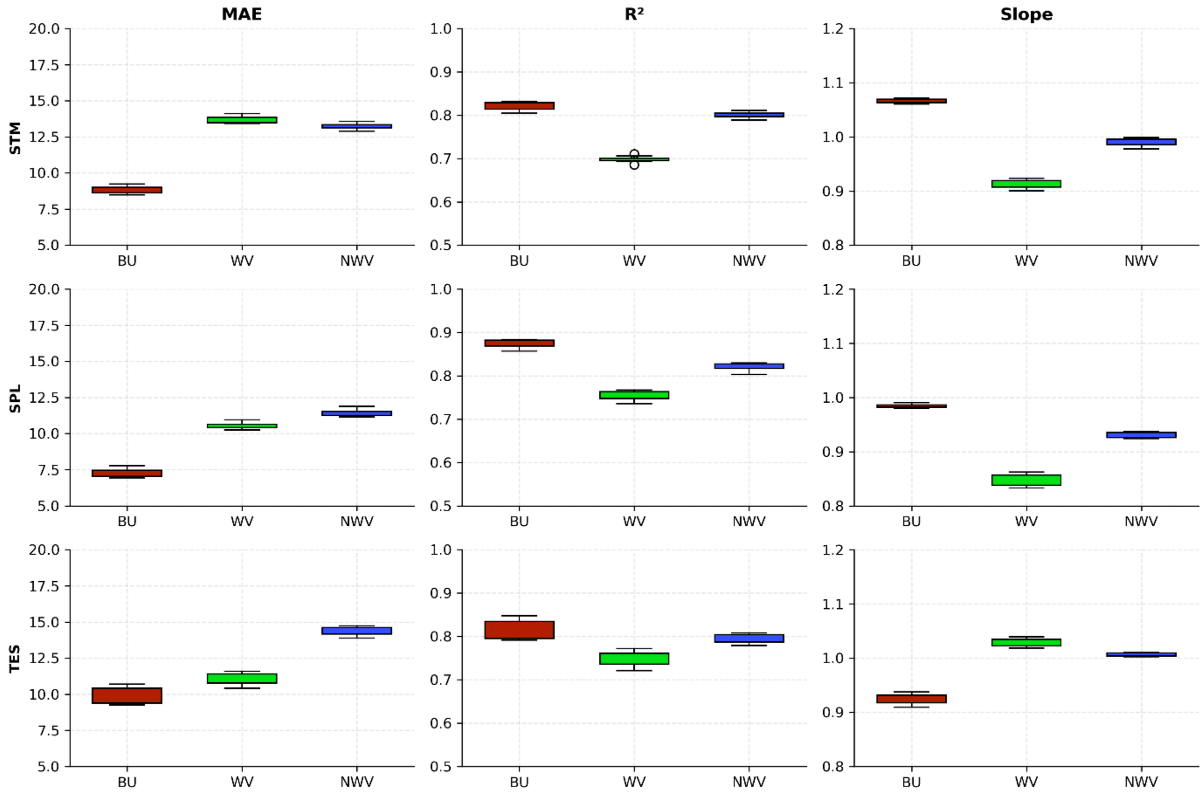

Figure-SI 4 Variability in model performance when the validation point grid is shifted by one point (ca. 3.30 m) in each of eight directions (Queen contiguity) to account for geolocation errors of Sentinel- and Google Earth VHR data. Model: Same-year model of 2024. Each boxplot represents nine values (default position plus eight shifted positions). The greater the spread, the higher the possible effect of geolocation errors on the model performance. BU: Built-up surfaces, WV: Woody vegetation, NWV: Non-woody vegetation. STM: Spectral-temporal metrics, SPL: Spline coefficients, TES: TESSERA latent embeddings.

4. Full validation results

Table-SI 3 Mean absolute errors (MAE) for models based on spectral-temporal metrics (STM), spline coefficients (SPL), and TESSERA latent embeddings (TES) for all three validated classes built-up surfaces (BU), woody vegetation (WV), and non-woody vegetation (NWV) for same-year, temporally transferred, and temporally generalized models.

	MAE	Train 2019			Train 2020			Train 2021			Train 2022			Train 2023			Train 2024			Generalized		
		STM	SPL	TES	STM	SPL	TES	STM	SPL	TES	STM	SPL	TES	STM	SPL	TES	STM	SPL	TES	STM	SPL	TES
Predict 2019	BU	12.4	**8.3**	11.3	11.5	**9.2**	10.5	8.8	**8.6**	10.8	**8.6**	8.7	10.4	**8.8**	9.0	11.8	10.2	**8.3**	11.0	**7.6**	**7.6**	9.5
	WV	15.9	**11.1**	13.0	19.0	13.3	**12.1**	14.0	**10.8**	12.9	14.1	**12.2**	13.5	14.7	**10.6**	11.4	13.4	**11.2**	12.2	14.1	**10.4**	12.5
	NWV	12.2	**12.1**	15.5	15.0	**14.0**	17.6	12.8	**12.4**	17.3	**13.4**	13.5	15.9	13.4	**12.9**	17.0	13.1	**12.4**	16.0	13.0	**11.3**	15.4
Predict 2020	BU	13.0	**10.0**	12.1	10.4	**7.9**	10.2	10.4	**8.2**	10.5	10.2	**8.9**	11.2	9.2	**8.3**	13.8	12.0	**8.8**	13.7	11.1	**7.6**	10.5
	WV	15.2	14.0	**12.8**	17.3	13.1	**12.8**	13.7	**10.4**	12.2	13.1	**11.3**	13.0	12.4	**11.4**	11.6	14.1	12.1	**11.5**	16.7	**9.5**	11.7
	NWV	**12.2**	14.1	15.0	**13.5**	13.6	17.2	**11.7**	11.8	15.2	**11.8**	13.4	14.4	**11.7**	13.0	17.2	12.7	**12.1**	16.1	12.4	**10.8**	15.0
Predict 2021	BU	13.4	**10.3**	11.7	11.6	**8.5**	12.0	8.9	**7.8**	9.7	**8.9**	9.0	11.6	9.0	**8.1**	13.4	10.1	**8.8**	13.6	9.1	**7.3**	9.5
	WV	16.7	14.5	**11.7**	18.8	14.1	**10.3**	13.9	**11.7**	12.5	13.3	14.4	**13.1**	14.3	11.2	**10.7**	12.9	11.6	**10.4**	15.8	**11.1**	11.6
	NWV	**12.8**	13.7	14.7	14.9	**14.1**	17.1	12.8	**12.5**	16.7	**12.7**	15.0	16.2	13.2	**12.9**	17.3	13.1	**12.3**	15.5	12.9	**11.9**	15.4
Predict 2022	BU	13.5	**9.4**	12.0	12.7	**8.6**	11.1	9.2	**7.3**	10.1	8.2	**7.5**	10.1	8.7	**7.1**	12.9	10.4	**8.1**	10.8	7.2	**6.7**	9.2
	WV	16.3	14.2	**12.2**	19.6	15.1	**11.3**	14.9	**11.1**	12.3	14.2	**11.1**	12.1	13.7	**9.3**	10.1	12.7	10.7	**9.8**	14.0	**10.2**	11.8
	NWV	**12.6**	13.2	15.7	**14.6**	15.0	17.4	12.9	**12.3**	17.1	12.8	**12.0**	16.0	12.2	**10.7**	16.9	12.1	**11.3**	13.3	12.4	**10.9**	15.4
Predict 2023	BU	15.5	**9.2**	11.5	14.6	**8.0**	10.2	10.5	**7.9**	8.9	10.1	**7.4**	10.5	9.6	**6.9**	11.6	11.7	**7.5**	10.5	10.1	**6.1**	8.8
	WV	18.4	13.3	**13.0**	21.3	13.9	**11.0**	15.0	13.0	**12.4**	14.9	**11.9**	12.1	14.3	10.8	**10.3**	14.5	10.6	**10.4**	16.2	**10.1**	12.5
	NWV	15.1	**13.2**	15.7	16.0	**14.1**	16.3	**13.1**	14.9	16.5	13.2	**13.1**	15.9	**11.9**	12.2	16.2	13.1	**11.4**	14.5	12.2	**11.3**	15.0
Predict 2024	BU	15.0	**10.5**	13.6	15.9	**8.7**	12.2	10.8	**7.6**	10.9	10.2	**7.7**	9.9	10.7	**8.0**	10.8	8.6	**6.9**	9.8	8.3	**6.3**	9.0
	WV	18.4	14.7	**11.9**	23.8	18.0	**11.9**	18.0	**13.3**	**13.3**	17.6	14.4	**14.2**	16.3	12.4	**11.5**	13.4	**10.3**	10.8	16.3	**10.6**	12.6
	NWV	14.4	**13.7**	15.2	**16.3**	17.4	18.0	15.4	**14.0**	19.0	**14.9**	15.5	18.8	14.5	**13.4**	18.5	12.9	**11.2**	14.2	13.9	**10.7**	15.5

Table-SI 4 Coefficients of determination (R^2) for models based on spectral-temporal metrics (STM), spline coefficients (SPL), and TESSERA latent embeddings (TES) for all three validated classes built-up surfaces (BU), woody vegetation (WV), and non-woody vegetation (NWV) for same-year, temporally transferred, and temporally generalized models.

R^2		**Train 2019**			**Train 2020**			**Train 2021**			**Train 2022**			**Train 2023**			**Train 2024**			**Generalized**		
		STM	SPL	TES	STM	SPL	TES	STM	SPL	TES	STM	SPL	TES	STM	SPL	TES	STM	SPL	TES	STM	SPL	TES
Predict 2019	BU	0.74	**0.84**	0.77	0.75	0.79	**0.81**	**0.83**	**0.83**	0.80	**0.85**	0.84	0.80	**0.82**	0.81	0.79	0.80	**0.85**	0.80	0.84	**0.86**	0.81
	WV	0.61	**0.76**	0.70	0.59	**0.70**	**0.70**	0.69	**0.72**	0.69	**0.70**	**0.70**	0.68	0.61	**0.73**	**0.73**	0.66	**0.71**	**0.71**	0.71	**0.77**	0.73
	NWV	0.81	**0.82**	0.77	0.77	**0.80**	0.74	**0.83**	0.80	0.73	**0.82**	0.77	0.74	**0.79**	0.78	0.77	**0.80**	**0.80**	0.77	0.83	**0.84**	0.78
Predict 2020	BU	0.74	**0.80**	0.74	0.79	**0.85**	0.79	0.80	**0.85**	0.80	0.81	**0.84**	0.79	0.81	**0.84**	0.76	0.78	**0.84**	0.76	0.78	**0.86**	0.79
	WV	0.58	**0.71**	**0.71**	0.61	**0.72**	0.70	0.67	**0.72**	0.69	0.70	**0.72**	0.70	0.69	**0.73**	0.71	0.62	0.68	**0.71**	0.60	**0.81**	0.72
	NWV	**0.80**	0.77	0.78	0.79	**0.80**	0.76	**0.82**	0.80	0.75	**0.82**	0.77	0.77	**0.81**	0.79	0.77	0.77	**0.80**	0.79	0.82	**0.86**	0.79
Predict 2021	BU	0.72	**0.83**	0.78	0.75	**0.84**	0.80	0.83	**0.85**	0.81	**0.84**	**0.84**	0.81	0.81	**0.84**	0.79	0.82	**0.83**	0.79	0.82	**0.87**	0.82
	WV	0.53	0.67	**0.74**	0.57	0.69	**0.74**	0.67	**0.73**	0.71	0.69	**0.71**	**0.71**	0.58	0.73	**0.75**	0.64	0.66	**0.75**	0.64	**0.77**	0.74
	NWV	0.77	0.77	**0.78**	0.76	**0.80**	0.75	0.80	**0.81**	0.75	**0.81**	0.78	0.75	0.76	**0.79**	0.77	0.78	0.78	**0.79**	0.81	**0.84**	0.79
Predict 2022	BU	0.72	**0.82**	0.79	0.73	**0.82**	**0.82**	0.84	**0.87**	0.82	**0.87**	**0.87**	0.82	0.84	**0.86**	0.81	0.81	**0.85**	0.83	0.87	**0.88**	0.83
	WV	0.51	0.67	**0.73**	0.54	0.68	**0.72**	0.67	**0.74**	0.71	0.69	**0.76**	0.73	0.64	**0.79**	0.77	0.65	0.70	**0.78**	0.69	**0.80**	0.74
	NWV	0.77	**0.79**	0.78	0.77	**0.80**	0.75	**0.81**	**0.81**	0.74	**0.82**	**0.82**	0.77	0.81	**0.83**	0.77	**0.81**	**0.81**	**0.81**	0.83	**0.86**	0.80
Predict 2023	BU	0.66	**0.84**	0.79	0.67	**0.85**	0.82	0.82	**0.85**	0.84	0.84	**0.87**	0.82	0.83	**0.88**	0.81	0.78	**0.87**	0.82	0.80	**0.90**	0.83
	WV	0.40	0.70	**0.71**	0.56	0.71	**0.73**	0.69	**0.72**	**0.72**	0.69	**0.74**	0.71	0.68	**0.79**	0.77	0.66	0.74	**0.76**	0.65	**0.81**	0.73
	NWV	0.69	**0.79**	0.76	0.77	**0.81**	0.76	**0.81**	0.79	0.75	0.81	**0.82**	0.76	0.82	**0.83**	0.79	0.79	**0.83**	0.81	0.83	**0.86**	0.79
Predict 2024	BU	0.70	**0.82**	0.78	0.65	**0.82**	0.80	0.80	**0.86**	0.78	0.81	**0.87**	0.80	0.78	**0.84**	0.77	0.83	**0.88**	0.82	0.83	**0.90**	0.82
	WV	0.44	0.70	**0.73**	0.53	0.66	**0.69**	0.63	**0.71**	0.70	0.66	**0.73**	0.66	0.61	**0.75**	0.74	0.71	**0.77**	0.76	0.67	**0.80**	0.73
	NWV	0.71	**0.78**	**0.78**	0.74	**0.75**	0.73	0.78	**0.79**	0.74	**0.79**	0.78	0.72	0.73	**0.78**	0.76	0.81	**0.83**	0.80	0.82	**0.86**	0.79

Table-SI 5 Slopes for models based on spectral-temporal metrics (STM), spline coefficients (SPL), and TESSERA latent embeddings (TES) for all three validated classes built-up surfaces (BU), woody vegetation (WV), and non-woody vegetation (NWV) for same-year, temporally transferred, and temporally generalized models.

	Slope	**Train 2019**			**Train 2020**			**Train 2021**			**Train 2022**			**Train 2023**			**Train 2024**			**Generalized**		
		STM	SPL	TES	STM	SPL	TES	STM	SPL	TES	STM	SPL	TES	STM	SPL	TES	STM	SPL	TES	STM	SPL	TES
Predict 2019	BU	1.13	**1.04**	0.84	1.11	**0.98**	0.91	1.08	**0.96**	0.95	1.11	1.09	**0.92**	1.05	**1.01**	0.93	1.13	**1.02**	0.96	0.96	**0.99**	0.88
	WV	0.81	**0.89**	0.85	0.80	0.83	**1.01**	0.89	0.87	**0.97**	**0.91**	0.86	0.89	0.82	0.88	**1.01**	0.97	0.83	**1.00**	0.78	0.86	**0.88**
	NWV	0.92	**0.93**	0.92	**0.96**	0.90	0.95	0.95	0.94	**0.96**	**0.99**	0.93	0.92	0.94	0.92	**1.00**	0.97	0.90	**0.99**	0.86	**0.91**	0.89
Predict 2020	BU	1.19	**1.07**	0.84	1.08	**0.97**	0.89	1.11	**0.97**	0.92	1.16	**1.05**	**0.95**	**1.03**	**1.03**	0.92	1.20	1.01	**1.00**	1.08	**0.94**	0.86
	WV	**0.84**	0.83	0.83	0.80	0.82	**0.88**	0.86	0.86	**0.94**	**0.96**	0.88	0.88	0.87	0.85	**1.01**	0.90	0.77	**0.97**	0.70	**0.86**	**0.86**
	NWV	0.90	**0.93**	0.91	0.90	0.91	**0.93**	0.93	0.90	**0.95**	**0.98**	0.93	0.93	0.93	0.94	**1.03**	0.92	0.90	**1.00**	0.82	**0.91**	0.88
Predict 2021	BU	1.19	**1.12**	0.86	1.12	**1.00**	0.89	1.09	**0.97**	0.91	1.12	1.08	**0.94**	1.04	**1.02**	0.97	1.15	1.01	**1.00**	**1.03**	0.96	0.89
	WV	0.79	0.86	**0.88**	0.81	0.83	**1.00**	0.86	0.83	**0.89**	0.90	0.85	**0.92**	0.82	0.87	**1.03**	0.95	0.87	**1.03**	0.73	0.84	**0.88**
	NWV	0.90	**0.93**	0.92	**0.94**	0.92	0.92	0.92	0.91	**0.94**	**0.96**	**0.96**	0.93	0.92	0.95	**1.03**	0.94	0.95	**1.00**	0.85	0.88	**0.91**
Predict 2022	BU	1.18	**1.06**	0.84	1.15	**0.99**	0.89	1.10	**0.98**	0.96	1.11	**1.00**	0.88	1.06	**0.98**	0.92	1.17	**0.99**	0.92	0.96	**0.97**	0.89
	WV	0.81	0.84	**0.86**	0.76	0.82	**0.96**	0.84	0.85	**0.94**	**0.88**	**0.88**	0.85	0.83	0.91	**1.00**	0.95	0.87	**1.02**	0.76	**0.87**	**0.87**
	NWV	0.91	**0.95**	0.91	**0.94**	**0.94**	0.93	0.92	**0.93**	**0.93**	**0.94**	0.93	0.91	0.92	0.95	**0.96**	0.93	0.91	**0.96**	0.84	**0.90**	**0.90**
Predict 2023	BU	1.24	**1.08**	0.85	1.19	**1.00**	0.91	1.16	**0.98**	0.97	1.17	**1.02**	0.90	1.11	**1.00**	0.94	1.21	**1.03**	0.92	1.04	**1.00**	0.90
	WV	0.75	**0.88**	0.85	0.76	0.84	**1.03**	0.89	0.84	**0.98**	0.91	**0.92**	0.88	0.85	0.90	**0.97**	0.95	0.85	**0.98**	0.74	**0.91**	0.86
	NWV	0.89	**0.96**	0.91	**0.97**	0.96	0.96	0.96	**0.98**	0.94	**0.97**	**0.97**	0.93	0.94	0.94	**0.96**	0.97	0.92	**1.02**	0.88	**0.93**	0.89
Predict 2024	BU	1.27	**1.14**	0.84	1.30	**1.02**	0.91	1.17	1.02	**1.01**	1.15	**1.06**	0.93	1.14	**1.02**	0.97	1.07	**0.99**	0.93	0.96	**1.00**	0.91
	WV	0.77	0.88	**0.89**	0.74	0.81	**1.13**	0.80	0.80	**0.97**	0.83	**0.89**	0.86	0.77	0.88	**1.07**	0.92	0.86	**1.04**	0.73	**0.91**	**0.91**
	NWV	0.95	**0.97**	0.94	0.98	0.96	**0.99**	0.95	0.97	**1.00**	0.99	**1.00**	0.98	0.96	1.01	**1.00**	**0.99**	0.94	**1.01**	0.85	**0.96**	0.94

5. Class-wise results aggregated by year of training and year of prediction

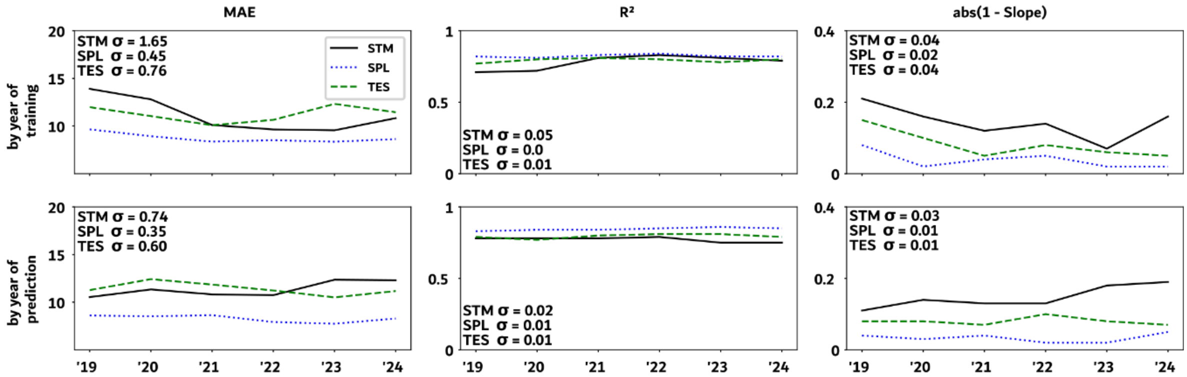

Figure-SI 5 For built-up surfaces: Mean absolute error (a), coefficient of determination (b), and Slope (c) for all years, aggregated by year of training (top) and year of prediction (bottom). STM: Spectral-temporal metrics, SPL: Spline coefficients, TES: TESSERA latent embeddings, σ: Standard deviation.

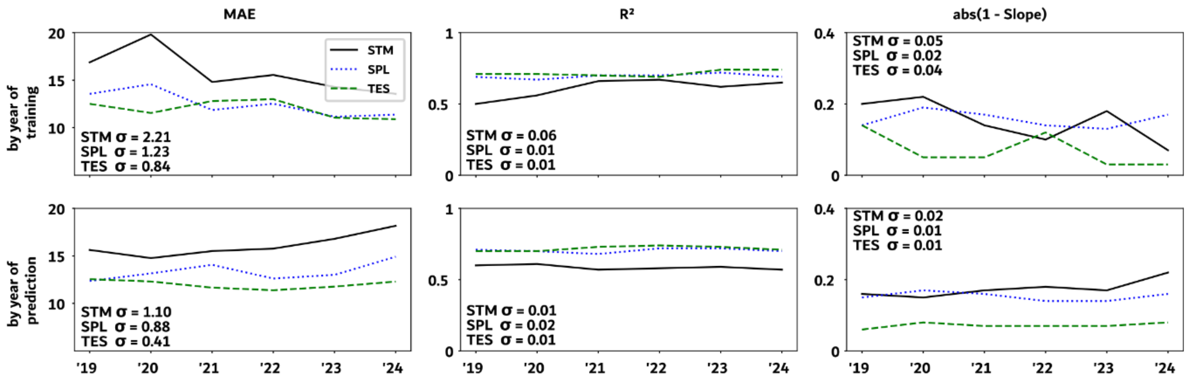

Figure-SI 6 For woody vegetation: Mean absolute error (a), coefficient of determination (b), and Slope (c) for all years, aggregated by year of training (top) and year of prediction (bottom). STM: Spectral-temporal metrics, SPL: Spline coefficients, TES: TESSERA latent embeddings, σ: Standard deviation.

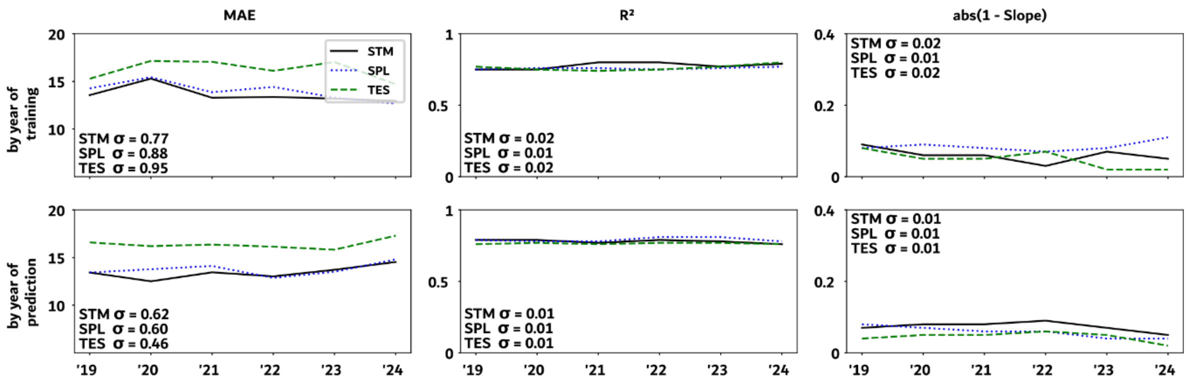

Figure-SI 7 For non-woody vegetation: Mean absolute error (a), coefficient of determination (b), and Slope (c) for all years, aggregated by year of training (top) and year of prediction (bottom). STM: Spectral-temporal metrics, SPL: Spline coefficients, TES: TESSERA latent embeddings, σ: Standard deviation.

References

Rowland, C. S.; Marston, C. G.; O'Neil, A. W. (2025): Land Cover Map 2024 (10m classified pixels, GB). With assistance of C. G. Marston, UK Centre for Ecology & Hydrology, NERC EDS Environmental Information Data Centre.